# NANOSCALE THERMOMETRY OF A PROTOTYPE HARD DISK HEAD

## SVEN BODENSTEDT



# **Master Thesis**

1<sup>st</sup> Supervisor: Prof. Dr. Jörg Wrachtrup 2<sup>nd</sup> Supervisor: Prof. Dr. Peter Michler

3<sup>rd</sup> Physics Institute Faculty 8: Mathematics and Physics University of Stuttgart

December 2017



State of the art hard disk recording heads use nanoscopic magnetic fields to encode digital data as magnetization in small sectors on a recording medium. The high field amplitudes combined with fast switching times and large gradients make these devices interesting for applications unrelated to digital storage technology.

In this thesis the capabilities of a conventional hard disk head or more specifically its writer as a manipulation tool for a single or multiple spins are demonstrated. A suitable system for the experiments is the solid state spin system of the nitrogen-vacancy center in diamond.

The experiments make use of the writer's high field strength to establish control fields with amplitudes of several hundreds of milliteslas. Combined with the high bandwidth these fields can be pulsed within nanoseconds and hence faster than a typical measurement. The bandwidth is also sufficient to use the writer as a microwave emitter to drive extremely fast transitions resonantly or to drive nonadiabatic fast passages. Moreover, the gradient can be used to address individual spins on the nanoscale.

Apart from conventional hard disc drives this thesis also deals with studies on heat assisted magnetic recording heads. This innovative technology is supposed to further reduce the bits' physical size but is not yet available in commercial drives. It has the potential to further increase the storage capacities for prospective devices.

The development of these prototypes hinges on suitable sensors for the nanoscale characterization of the produced heat and magnetic field. Individual nitrogen-vacancy centers in diamond are potential candidates for this task. They are both efficient single-spin magnetometers and sensitive temperature sensors on an atomic scale. This thesis investigates and evaluates the potential of the nitrogen-vacancy center as a nanoscale thermo- and magnetometer for the hard disk industry.

Modernste Festplattenschreibköpfe verwenden auf wenige Nanometer fokussierte Magnetfelder, um digitale Information als Magnetisierung in kleinen Sektoren auf einem Speichermedium zu schreiben. Hohen Feldamplituden in Verbindung mit schnellen Schaltzeiten und großen Gradienten machen Festplatten für Anwendungen über die digitale Speichertechnik hinaus interessant.

In dieser Arbeit werden die Möglichkeiten konventioneller Festplatten oder genauer gesagt des Schreibkopfes als Werkzeug für die Manipulierung von einzelnen oder mehreren Spins aufgezeigt. Ein geeignetes System für diese Experimente ist das Stickstoff-Fehlstellen-Zentrum in Diamant

Die Experimente nutzen die hohe Feldstärke des Schreibkopfes für Kontrollfelder mit Amplituden von mehreren hundert Millitesla. In Verbindung mit der hohen Bandbreite können diese Felder innerhalb von Nanosekunden geschalten werden und somit schneller als die Dauer einer gewöhnlichen Messung. Die Bandbreite ist darüber hinaus ausreichend für die Verwendung des Schreibkopfes als Mikrowellen Sender, um extrem schnelle Übergänge oder schnelle nichtadiabatische Passagen zu treiben. Darüber hinaus kann der Gradient benutzt werden, um einzelne Spins mit Abständen von nur wenigen Nanometern zu adressieren.

Abgesehen von gewöhnlichen Festplattenköpfen behandelt diese Arbeit auch Untersuchungen über Schreibköpfe, die heat assisted magnetic recording verwenden. Diese noch nicht kommerziell erhältliche neue Technologie hat das Potential hat, die physikalische Größe der Bits weiter zu verkleinern und die Speicherkapazität zukünftiger Geräte deutlich zu erhöhen.

Die Entwicklung dieser Prototypen ist abhängig von geeigneten Sensoren, die auf Nanometer genau die erzeugte Hitze und Magnetfelder charakterisieren können. Stickstoff-Fehlstellen-Zentren in Diamant sind mögliche Kandidaten für diese Aufgabe. Sie sind sowohl effiziente Magnetfeldsensoren basierend auf einzelnen Spins, als auch sensitive Temperatursensoren im atomaren Bereich. Diese Arbeit untersucht und bewertet das Potential einzelner Stickstoff-Fehlstellen-Zentren als Nanometer genaues Thermo- und Magnetometer für die Festplattenindustrie.

\_\_\_\_\_

I am grateful to my supervisor Prof. Dr. Jörg Wrachtrup who affords me to work on these interesting and exciting projects and to my second supervisor Prof. Dr. Peter Michler for the insightful comments during my reports. I would also like to thank my mentor Ingmar Jakobi for his great collaboration and assistance during the whole experiments. I would particularly like to thank him for his support by revising my thesis and providing me with the rendered figures. Special thanks go to Philipp Neumann for sharing his experience and his advice.

This thesis would not have been possible without the support of Rolf Reuter, who prepared the nanodiamond samples and instructed me in handling the nanocrystalline diamonds. I would also like to thank Ilja Gerhardt for his valuable ideas. I thank Adrej Denisenko and Ali Momenzadeh for preparation of the bulk diamond samples.

Many thanks go to Thomas Öckinghaus for recording the AFM scan for my thesis. My special thanks go to Thorsten Rendler who always had a ready answer to my questions. I also thank Julia Michl, Dominik Schmid-Lorch, Florestan Ziem, Philipp Konzelmann, Jakob Steiner, Stefan Jesenski and the whole Pneumann group for the valuable discussions.

This thesis would have also not been possible without the support of Seagate Technoloy PLC. My special thanks go to Fadi El Hallak for providing me and instructing me about the prototype HAMR heads. I also thank Patrick Fletcher for the help on operating the heads.

I owe my deepest gratitude to my friends and family, especially to my parents who are always an inspiration and make a major contribution to my successful studies.

# CONTENTS

_ In	atroduction 1					
1	EXPERIMENTAL SYSTEM 3					
1	NITROGEN-VACANCY CENTER IN DIAMOND 5					
	1.1 Properties of the Nitrogen-Vacancy Center 5					
	1.2 Hamiltonian of the Electronic Ground State 6					
	1.3 Control and Read-Out 8					
	1.4 Magnetometry 9					
	1.5 Thermometry 10					
2 FERROMAGNETISM 13						
	2.1 Terminology 13					
	2.2 Permeability 14					
	2.3 Hysteresis 15					
	2.4 Magnetic Domains 16					
3						
	3.1 Objective and Hard Disk Head Scan 17					
	3.2 Spin Initialization, Read-Out and Control 17					
	3.3 Samples 18					
	3.4 Modifications for Nanodiamonds 19					
	3.5 Hard Disc Heads 19					
ii	CONVENTIONAL HARD DISK HEAD 21					
4	FUNCTIONAL PRINCIPLE OF CONVENTIONAL HARD DISK					
	DRIVES 23					
	4.1 Structure of a Conventional Hard Disk Drive 23					
	4.2 The Write Field 24					
	4.3 Beyond Data Storage 26					
5	STATE OF RESEARCH 27					
	5.1 Photo Luminescence Imaging 27					
	5.2 Spin Magnetometry 27					
6 PASSIVE OPERATION 29						
	6.1 Writer Positioning 29					
	6.2 Remanence Magnetization 30					
	6.3 Time Resolved Photo Luminescence Response 31					
	6.4 Drive Field Amplification 32					
	6.5 Spin Relaxation Times 33					
7	ADVANCED ACTIVE APPLICATIONS 37					
	7.1 Pulsed ODMR 37					
	7.2 Magnetic Field Imaging 38					
	7.3 Spectral Addressing 39					
	7.4 Drive Field Antenna 41					
	7.5 Nonadiabatic Fast Passage 45					

```
7.6 Outlook
iii HEAT ASSISTED MAGNETIC RECORDING
  FUNCTIONAL PRINCIPLE OF HAMR DEVICES
  8.1 Basic Principle of Heat Assisted Magnetic Recording
                                                        51
  8.2 Near Field Transducer
  AIRBRUSHED NANODIAMONDS
                                   55
       Temperature Measurement of the Gold Lollipop
       Approaches for A Nanoscale Temperature Measure-
       ment
               56
   9.3 Spin Coating
                      58
   9.4 Airbrushing
                     59
   9.5 Characterization of Nanodiamonds
                                         60
10 NANOSCALE THERMOMETRY
   10.1 HAMR Head Preparation
                                 63
   10.2 Photo Luminescence of the Near Field Transducer
                                                      63
   10.3 Results
                 64
   10.4 Outlook
                  67
CONCLUSION
                69
  APPENDIX
                71
  MAGNETIC FIELD RECONSTRUCTION
                                        73
  HARMONIC GENERATION
       Second and Third Harmonic Generation
       Difference and Sum Frequency Generation
BIBLIOGRAPHY
                 77
```

#### **ACRONYMS**

ABS air-bearing surface

AC alternating current

AFM atomic force microscope

APD avalanche photodiode

AWG arbitrary waveform generator

BPMR bit patterned magnetic recording

CVD chemical vapor deposition

DC direct current

**DESM** deterministic emitter switch microscopy

FEM finite element method

FID free induction decay

FWHM full width at half maximum

HAMR heat assisted magnetic recording

HDD hard disk drive

**HGA** head gimbal assembly

ISC intersystem crossing

LAC level-anti-crossing

MAMR microwave assisted magnetic recording

MAS microwave assisted switching

MRI magnetic resonance imaging

NA numerical aperture

ND nanodiamond

NFT near field transducer

NV nitrogen-vacancy center

**ODMR** optically detected magnetic resonance

PL photo luminescence

PMR perpendicular magnetic recording

PVA polyvinyl alcohol

qubit quantum bit

**R&D** research and development

rpm rotations per minute

SMR shingled magnetic recording

**SNR** signal-to-noise ratio

SP surface plasmon

SThM scanning thermal microscope

TDMR two-dimensional magnetic recording

**ZFS** zero field splitting

ZPL zero-phonon line

Spin systems have become an important field of interest in fundamental as well as in applied research. They are used to demonstrate fundamental quantum mechanical effects such as quantum teleportation [1] or violation of the temporal Bell inequalities [2]. The demonstration of quantum error correction [3] is considerable for quantum information processing and communication. Material research profits from spin based sensors by measuring the material properties as for instance the thermal conductivity [4], crystal defect orientations [5] and domain-wall hoppings [6] on the nanoscale. Spin based sensors can also give a contribution to biophysical research. They can used to detect single-neuron action potentials [7], to measure the temperature inside living cells [8] or to do magnetic spin imaging with subcellular resolution [9].

A crucial property of a spin based quantum bit (qubit) or sensor system is the ability to perform coherent operations on individual spins. The fact that a spin couples efficiently to a magnetic field can be used to manipulate its state. Therefore the capability of creating strong, fast and local magnetic fields is of wide interest.

Commercially available hard disk drives (HDDs) combine these features for well over thirty years now in their magnetic write heads. Instead of writing digital information by switching the direction of a focused magnetic field these writers could be used to control the dynamics of a spin system.

The system chosen to investigate the abilities of hard disc drives for spin physic experiments is the nitrogen-vacancy center (NV) in diamond [10]. With the NV several experiments regarding magnetic field measurement [11] and imaging [12], as well as electric field [13], pH [14], temperature [15], spectroscopy [16, 17] or magnetic resonance imaging (MRI) [18] measurements have been performed. The NV can be used both as a sensor for physical properties of the HDD write head and as a target for control operations by the writer.

This thesis is divided into three parts. The experimental system including a short introduction to the NV (Chapter 1), ferromagnetism (Chapter 2) and the setup (Chapter 3) is described in Part i. Part ii is about the functional principle (Chapter 4) and characterization (Chapter 5 and Chapter 6) of conventional hard disk heads and the ability to use them for spin manipulation (Chapter 5 and Chapter 7).

The last part (Part iii) deals with a new generation of HDDs. Beyond introducing the basic working principle (Chapter 8) a new method for homogeneously distributing nanodiamonds (NDs) on profiled surfaces (Chapter 9) is demonstrated. In the last chapter (Chapter 10)

# 2 ACRONYMS

results for a characterization of hard disc head prototypes based on nanoscale temperature measurements are shown.

# Part I EXPERIMENTAL SYSTEM

NITROGEN-VACANCY CENTER IN DIAMOND

Diamond is a material well known for its usage as gem stones for jewelries or as a cutting material for industrial or medical tools. Natural diamonds can be formed in the earth's mantle at high temperatures and pressure under extraordinary conditions making them rare and expensive. Nowadays they can also be produced synthetically on a large scale for scientific or industrial applications.

Diamond is one of the hardest known materials and has an extraordinary high thermal conductivity. These exceptional physical properties arise from carbon atoms arranged in a face-centered cubic crystal lattice (diamond lattice).

#### 1.1 PROPERTIES OF THE NITROGEN-VACANCY CENTER

The lattice can hold a wide variety of defects. Some of these can be fluorescent affecting the diamond's color. That is why some of the defects are called color centers.

The NV is a color defect in the diamond lattice, where two adjacent carbon atoms are replaced by a nitrogen atom and a vacancy (see Figure 1 a) The zero-phonon line (ZPL) at 637 nm leads to a pink color of diamonds with a high NV density.

The NV has three dominant charge states, namely the neutral NV<sup>o</sup>, the positively charged NV<sup>+</sup> and the negatively charged NV<sup>-</sup> [19, 20]. This thesis focuses on the negatively charged NV<sup>-</sup> state (minus sign is omitted from now on) corresponding to six electrons locally concentrated at the position of the vacancy.

The electronic level structure can be deduced by exploiting the defect's  $C_{3v}$  symmetry using group theoretical methods [21]. Both the electronic ground state  ${}^{3}A_{2}$  and the excited state  ${}^{3}E$  1.945 eV (637 nm) above the ground state are triplet states [22].

At room temperature the system can be off-resonantly exited by green laser light into a phonon sideband. The excited state can decay either optically by emitting a red-shifted photon (see Figure 1) or non-radiative via meta-stable singlet states ( ${}^{1}A_{1}$  and  ${}^{1}E$ ).

An important property of the NV is its total electron spin. Since two of the six electrons are unpaired the triplet states correspond to a total spin quantum number of S=1 whereas the singlet states have S=0. The non-vanishing total electron spin makes the NV electron ground state sensitive for magnetic fields.

The connecting line between the nitrogen atom and the vacancy defines a symmetry axis (NV-axis). The three-dimensional coordinate

system used from now on can be defined with its *z*-axis parallel to the NV-axis. Since the orientations of *x*- and *y*-axis are not relevant for this thesis, they can be chosen in an arbitrary way perpendicular to themselves and the *z*-axis.

#### 1.2 HAMILTONIAN OF THE ELECTRONIC GROUND STATE

The spin Hamiltonian describing the electronic ground state in a simplified form is given by [24]

$$\hat{H}_{0} = \hat{H}_{ZFS} + \hat{H}_{Zeeman} = D(T)\hat{S}_{z}^{2} + \gamma_{e} \left(B_{x}\hat{S}_{x} + B_{y}\hat{S}_{y} + B_{z}\hat{S}_{z}\right) . (1)$$

The spin matrices for the S=1 configuration system are here defined as

$$\hat{S}_{x} = \frac{\hbar}{\sqrt{2}} \begin{pmatrix} 0 & 1 & 0 \\ 1 & 0 & 1 \\ 0 & 1 & 0 \end{pmatrix}, \quad \hat{S}_{y} = \frac{\hbar}{\sqrt{2}} \begin{pmatrix} 0 & -i & 0 \\ i & 0 & -i \\ 0 & i & 0 \end{pmatrix} \quad \text{and}$$

$$\hat{S}_{z} = \hbar \begin{pmatrix} 1 & 0 & 0 \\ 0 & 0 & 0 \\ 0 & 0 & -1 \end{pmatrix} ,$$

$$(2)$$

with the reduced Planck constant  $\hbar = 1.055 \, \mathrm{J} \, \mathrm{s}$ .

This Hamiltonian can be separated into two parts: The first term  $\hat{H}_{ZFS}$  describes the electronic ground state in the absence of strain and magnetic fields ( $B_x = B_y = B_z = 0$ ). As in this special case the Hamiltonian commutes with  $\hat{S}_z$ , the quantum number  $m_s$  (describing the projection of the spin in the direction of the z-axis) is a good quantum number to describe the eigenstates of the system. For an S = 1 system  $m_s$  can attain the values -1, 0 or +1.

The parameter D =  $2.87\,\text{GHz} \cdot 2\pi\hbar^{-1}$  (at room temperature) corresponds to the so called zero field splitting (ZFS). In contrast to the NV, in free space the three eigenstates for S = 1 system are degenerated due to its isotropy. The NV's ZFS has its origin in the breaking of the axial symmetry due to the nitrogen atom leading to an abolition of the degeneracy even in the absence of magnetic fields. Consequently the  $m_s=0$  state is energetically lower than the  $m_s=\pm 1$  states.

The ZFS depends on both temperature T and crystal strain. The latter can even lead to an additional splitting between the  $m_s=1$  and  $m_s=-1$  states. The exact value can therefore vary for individual NVs depending on their environment.

The Hamiltonian's second term  $\hat{H}_{Zeeman}$  describes the behavior of the system under the influence of external magnetic fields. The gyromagnetic ratio  $\gamma_e = 2\pi \cdot 28.02 \, \text{GHz} \, \text{T}^{-1}$  is equivalent to the value for electrons in free space. The Zeeman splitting is isotropic in respect to the magnetic field components  $B_x$ ,  $B_y$  and  $B_z$ .

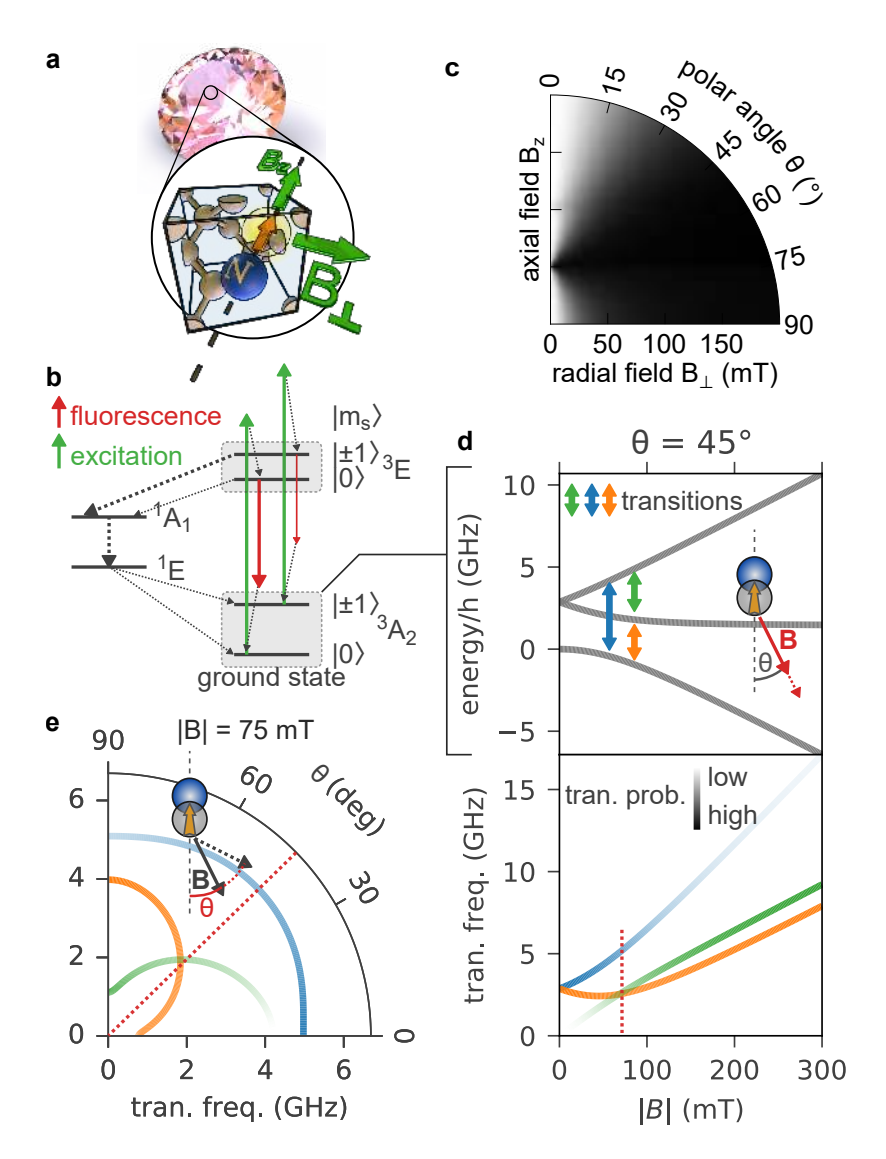


Figure 1: Description of the basic properties of the nitrogen-vacancy center (NV) center in diamond. a, position of nitrogen atom and vacancy in the diamond lattice. b, electron level scheme. c, NV's PL over magnetic field strength and orientation under saturated optical excitation (adopted from [23]). d, ground state levels (top) and transitions (bottom) over magnetic field strength with a fixed orientation of  $\theta=45^\circ$ . The transparency of the curves in the bottom graph describes the transition probability by the corresponding matrix element  $\langle f|\hat{H}_1|i\rangle$  for an unpolarized microwave control field. e, resonances over the orientation with a fixed magnetic field strength of |B|=75 mT. The transparency describes again the transition probabilities. The red dotted line in (d) and (e) highlights the eigenenergies at |B|=75 mT and  $\theta=45^\circ$  corresponding to the intersection of both graphs.

For magnetic fields aligned with the NV-axis the Hamiltonian commutes with  $\hat{S}_z$ . In this particular case the system can still be well described by the eigenvalues  $m_s$  of  $\hat{S}_z$ . For most experiments in this thesis the magnetic field has both arbitrary direction and field strength. In these situations the Hamiltonian usually does not commute with  $\hat{S}_z$ . Therefore the new eigenstates are superpositions of the original  $|m_s\rangle$  states.

#### 1.3 CONTROL AND READ-OUT

The optical excitation into the exited triplet state is spin conserving. The Hamiltonian describing the exited state is similar to the ground state except of a reduced ZFS of  $D_{ES} = 1.42 \, \text{GHz} \cdot 2\pi \hbar^{-1}$  (at room temperature) [25].

The decay of the exited state depends on the spin state: For  $m_s=0$  the radiative process is dominant, whereas for  $m_s=\pm 1$  the non-radiative decay via the meta-stable state is almost equally probable resulting in an intersystem crossing (ISC) between the triplet and singlet states (see Figure 1 b) [26]. The spin dependent decay paths in combination with the spin conserving excitation can be used both to initialize and read-out the spin state.

Beside optical excitation the electron spin state can be manipulated by alternating current (AC) magnetic fields. The whole system can be described by

$$\hat{H}_{total} = \hat{H}_0 + \cos(\omega t)\hat{H}_1 \tag{3}$$

with the time independent part  $\hat{H}_0$  (see Equation 1) and the oscillation part

$$\hat{H}_{1} = \gamma_{e} \left( B_{AC,x} \hat{S}_{x} + B_{AC,y} \hat{S}_{y} + B_{AC,z} \hat{S}_{z} \right) . \tag{4}$$

If the static magnetic field is aligned with the NV-axis ( $B_x = B_y = 0$ ,  $B_z \neq 0$ ) a resonant AC magnetic field perpendicular to the NV-axis ( $B_{AC,z} = 0$ ,  $B_{AC,\perp} = \sqrt{B_{AC,x}^2 + B_{AC,y}^2} \neq 0$ ) can drive coherent RABI oscillations, where the RABI frequency is proportional to the magnetic field amplitude  $B_{AC,\perp}$ . By adjusting the pulse length of the AC control field various type of control pulses (like  $\pi/2$ ,  $\pi$  or  $3\pi/2$  pulses) can be realized.

In general, the corresponding transition matrix element  $\langle f|\hat{H}_1|i\rangle$  depends on the initial  $|i\rangle$  and the final state  $|f\rangle$  and therefore on the strength and direction of the static magnetic field. Furthermore, it depends on  $\hat{H}_1$  corresponding to the polarization and amplitude of the AC magnetic control field.

#### 1.4 MAGNETOMETRY

Due to the system's symmetry it is often sufficient to describe the magnetic field by its aligned  $B_z$  and the respective orthogonal component  $B_\perp = \sqrt{B_x^2 + B_y^2}$ . The polar angle between  $B_z$  and  $B_\perp$  is defined as  $\theta = \arctan(B_\perp/B_z)$ . The absolute magnetic field strength |B| is given by  $|B| = \sqrt{B_\perp^2 + B_z^2} = \sqrt{B_x^2 + B_y^2 + B_z^2}$ .

The axial component of the electron spin  $m_s$  determines the NV's PL due to its different decay rates through the ISC. The superposition of  $|m_s\rangle$  states for non-aligned fields blurs the difference in PL brightness between the three eigenstates. The original bright  $m_s=0$  state has an increased probability to decay non-radiatively from the exited state resulting in a reduced PL.

Figure 1 (c) shows a simulation for the NV PL under saturated optical excitation depending on the magnetic field strength and direction. For a non-aligned magnetic field the PL is only half as bright compared to aligned fields. At about 50 mT the ZEEMAN splitting is in the same order as the ZFS of the excited state leading to a reduced PL due to the mixing of states even for a magnetic field parallel to the NV-axis. For non-saturated excitation the same effect occurs also at 102 mT, where the ZEEMAN term is in the same order as the ZFS of the ground state [27, 28].

The upper graph in Figure 1 (d) depicts the eigenenergies of the three spin states over the absolute value of the magnetic field |B| for a fixed angle  $\theta=45^\circ$ . For low magnetic field strengths ( $|B|\ll 100\, \text{mT}$ ) the level structure is dominated by the ZFS. By increasing the magnetic field far beyond 100 mT the ZFS becomes less important compared to the ZEEMAN term. The system can then be well described by the spin projection in the direction of the magnetic field instead of the direction of the NV-axis.

The bottom graph in Figure 1 (d) depicts the three resonances (blue, green and orange) between the energy levels. The transparency describes the transition matrix element  $\langle f|\hat{H}_1|i\rangle$  for an unpolarized microwave field at the NV. Therefor the transition probabilities for linear polarized microwave fields are simulated and averaged for evenly chosen polarization directions on the unit sphere.

In the low field regime the transition between the two upper levels (green) is forbidden ( $\langle f|\hat{H}_1|i\rangle=0$ ). For aligned fields this corresponds to the transition between the  $m_s=\pm 1$  states thus leading to  $|\Delta m_s|=2$ . This transition is forbidden by the selection rule  $|\Delta m_s|=1$ . With the same argument the transition between the lowest and highest level in the high field regime is forbidden, too.

Figure 1 (e) the resonances and transition probabilities are plotted over the angle of  $\theta$  for a fixed magnetic field strength of |B| = 75 mT. Especially the transition probability between the two upper levels (green) has a distinct dependence of the magnetic field orientation.

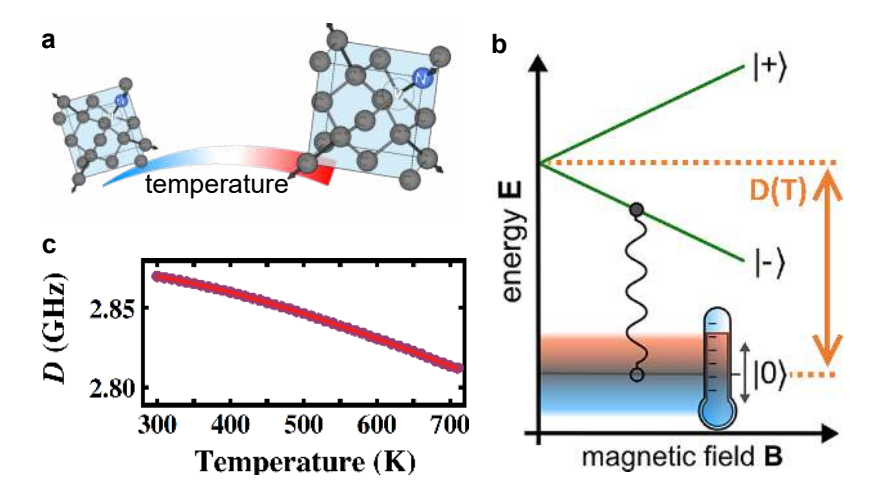


Figure 2: NV as a temperature sensor. **a**, temperature increase leads to lattice expansion. **b**, temperature dependent ZFS. At room temperature the derivation of the ZFS is about –80 kHz K<sup>-1</sup> (adopted from [15]). **c**, non-linear behavior of the ZFS for high temperatures of several hundreds of Kelvin (from [30]).

For perfectly aligned fields ( $\theta = 0^{\circ}$ ) the transition is forbidden by the selection rule while it is allowed for misaligned fields ( $\theta = 90^{\circ}$ ) due to spin state superposition.

If it is possible to determine the resonance frequencies for two of the three transitions the orthogonal ( $B_{\perp}$ ) and parallel ( $B_z$ ) component of the magnetic field can be reconstructed if the initialized state is known [12]. Due to the symmetry of the system the individual values for  $B_x$  and  $B_y$  cannot be calculated trivially. A more detailed analysis can be found in Appendix A.

To gain information about the azimuthal angle  $\varphi=\arctan(B_y/B_x)$  the symmetry of the system has to be broken. This can be achieved by an additional electric field [29] or by testing the explicit matrix elements with polarized microwave radiation.

#### 1.5 THERMOMETRY

By increasing the diamond's temperature the lattice expands (see Figure 2 a) and therefore increases the distance between nitrogen atom and vacancy. This leads to a decrease of the ZFS (see Figure 2 b) as the influence of the lattice confinement on the vacancy orbitals is reduced.

At room temperature an almost linear dependence of  $-80\,\mathrm{kHz}\,\mathrm{K}^{-1}$  can be observed [15] for the change of the ZFS with the temperature. This allows using an NV as a nanoscale temperature sensor. However for high temperatures above 400 K the linear approximation is

no longer applicable (see Figure 2 c). In the high temperature regime the ZFS splitting can be described by a third order polynomial

$$D(T) = a_0 + a_1 T + A_2 T^2 + A_3 T^3$$
 (5)

with the parameters  $a_0 = 2.87\,\text{GHz}$ ,  $a_1 = 9.7\cdot 10^{-5}\,\text{GHz}\,\text{K}^{-1}$ ,  $a_2 = -3.7\cdot 10^{-7}\,\text{GHz}\,\text{K}^{-2}$  and  $a_3 = 1.7\cdot 10^{-10}\,\text{GHz}\,\text{K}^{-3}$  [30]. Since the ZFS depends on the NV's environment, the exact parameters can vary for different NVs. This corresponds to the mentioned thermal shifts ranging from  $80\,\text{kHz}\,\text{K}^{-1}$  at 300 K up to 170 kHz K<sup>-1</sup> at 700 K.

An increase of the temperature also affects the NV's PL. For temperatures of about 700 K the PL has only a third of the brightness compared to room temperature [30]. In the same way the optically detected magnetic resonance (ODMR) contrast is drastically reduced at high temperatures.

Magnetism describes a fundamental class of physical effects. It is mediated by magnetic fields caused by electric currents or magnetic dipoles. Materials can be classified by their behavior in the presence of magnetic fields. Whereas diamagnetic materials are repelled by an external magnetic field, para- and ferromagnetic materials are attacked to it. Furthermore, ferromagnets have the feature of keeping their magnetization even in the absence of external magnetic fields. The magnetization describes the macroscopic collective orientation of intrinsic dipoles cause by unpaired spins.

Whereas the forces created by paramagnetism or diamagnetism are usually too weak to notice in everyday life, ferromagnetism is involved in many ordinary phenomena. Thus, compasses use the magnetic field produced by the Earth's outer core for navigation since the eleventh century.

Ferromagnetism is based on a quantum mechanical effect. Only for few materials the parallel alignment of their unpaired spins can be more stable than the anti-parallel alignment. The energy difference between these two configurations is called exchange energy. For ferromagnetic materials the exchange energy can be orders of magnitude greater than the magnetic dipole-dipole interaction.

#### 2.1 TERMINOLOGY

The magnetic properties of matter can be described by the macroscopic Maxwell equations

$$\operatorname{div}(\mathbf{B}) = 0 \tag{6a}$$

$$rot(\mathbf{H}) = \frac{\partial \mathbf{D}}{\partial t} + \mathbf{J}_f \tag{6b}$$

with the magnetic **B**-field and the current density of free charges  $J_f$ . The magnetic H-field is defined by  $\mathbf{H} = \frac{1}{\mu_0} \mathbf{B} - \mathbf{M}$  with the vacuum permeability  $\mu_0 = 4\pi \cdot 10^{-7} \, \text{N A}^{-2}$  and the macroscopic magnetization  $\mathbf{M} = \frac{d\mathbf{m}}{dV}$ . The latter is defined as the average density of magnetic moments  $\mathbf{m}$  per volume V. For pure magnetic effects the electric displacement field  $\mathbf{D}$  can be assumed as zero.

Figure 3 shows a schematic solution for the Maxwell equations for a homogeneously magnetized cylindrically shaped object (see subfigure c) surrounded by vacuum. Outside of the magnetized cylinder both magnetic fields are proportional with the vacuum permeability  $\mu_B$  as the proportionality factor. Inside the cylinder both fields differ in direction and amplitude.

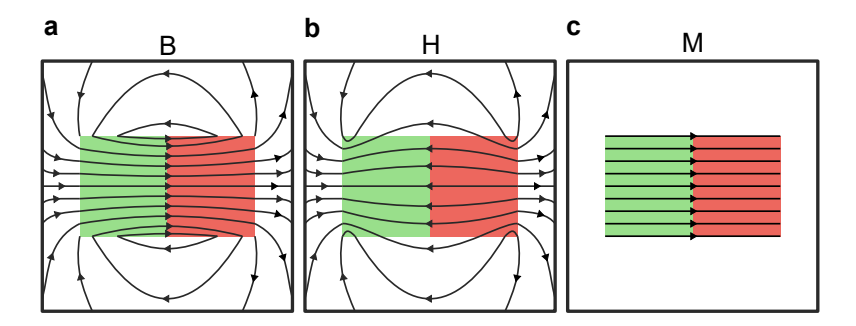


Figure 3: Schematic comparison of magnetic vector fields of a cylindrically shaped homogeneously magnetized object surrounded by vacuum. **a**, source-free magnetic B-field. **b**, magnetic H-field. Outside the material (in vacuum) H- and B-field point at the same direction. Within the magnetized material both fields point in opposite directions. **c**, homogeneous magnetization M of a cylindrically shaped object.

If a material is placed in a coil it is often useful to split up the **H**-field

$$\mathbf{H} = \mathbf{H}_0 + \mathbf{H}_d \tag{7}$$

into two independent parts. The first component  $H_0$  is used to describe the magnetic field created by the *free* currents, i. e. the current through the coil. The demagnetizing field  $\mathbf{H}_d$  stands for the magnetic field created by the *bound* currents, i. e. the locally bound currents inside the magnetized cylinder.

#### 2.2 PERMEABILITY

The magnetic permeability describes the ratio  $\mu = \frac{|B|}{|H|}$  between the magnetic **B**-field and the magnetic H-field. The relative permeability  $\mu_r = \frac{\mu}{\mu_0}$  is a dimensionless parameter to describe the permeability of a material. For ferromagnetic materials the relative permeability is much greater than 1.

Common ferromagnetic materials are iron (Fe), cobalt (Co), nickel (Ni) or metal alloys like mu-metal. The latter is an iron-nickel alloy whose relative permeability can reach values above 100 000. It can be integrated in coils to enhance the magnetic field of an electromagnet. It can also be used as a shield against static or low frequency magnetic fields.

The relative permeability is commonly stated for static magnetic fields. Usually it depends on the frequency and can even be complex, if phase shifts between **H**- and **B**-field are considered.

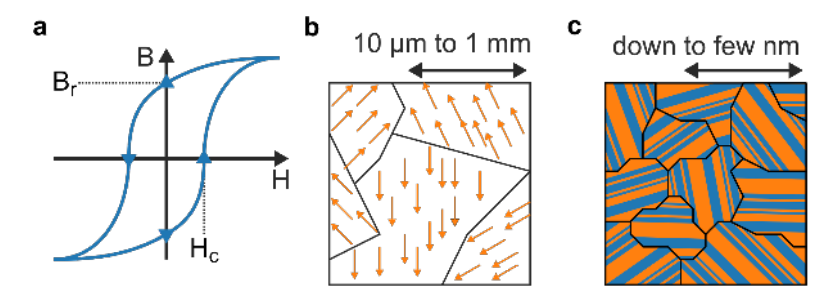


Figure 4: Important properties of ferromagnetic materials.  $\mathbf{a}$ , schematic graph of a hysteresis for a ferromagnetic material. Here  $B_r$  is the remanence magnetic  $\mathbf{B}$ -field and  $H_c$  the coercivity.  $\mathbf{b}$ , magnetic domains of a ferromagnet. The orange arrows indicate the direction of the magnetization of each domain.  $\mathbf{c}$ , grains of a polycrystalline ferromagnetic material. Different colors correspond to different orientations of the magnetization.

#### 2.3 HYSTERESIS

The relative permeability of a ferromagnetic material depends not only on the frequency, the temperature or the field strength but also on how the actual state is reached. Figure 4 (a) depicts that the behavior of the magnetic **B**-field differs depending on if the external magnetic **H**-field is in- (bottom curve) or decreased (top curve). This phenomenon is called the magnetic hysteresis of a ferromagnetic material. Consequently, the magnetic **B**-field and **H**-field do not have a simple linear dependency.

For large external H-fields the magnetization of the material saturates due to the finite number of unpaired spins. In the absence of an external magnetic H-field does not drop to zero. The remaining magnetic B-field is called the remanence field  $B_r$ .

The coercivity  $\mathbf{H}_c$  describes the magnetic  $\mathbf{H}$ -field needed to extinguish the remaining magnetization of the remanence. Beyond the coercivity the magnetization rises steeply with increasing magnetic  $\mathbf{H}$ -field. The coercivity therefore can be seen as an indicator for the minimum magnetic field strength needed to flip the magnetization of a ferromagnetic material.

Both parameters usually depend on the temperature. By rising the temperature typically the remanence magnetization as well as the coercivity diminish. Above the Curie temperature a ferromagnetic material loses its ferromagnetic properties.

The amplitude of the magnetic field needed to switch the magnetization (i.e. the coercivity  $\mathbf{H}_c$ ) can also be significantly reduced by simultaneously applying a microwave field perpendicular to the switching field. The effect of this microwave assisted switching (MAS) is deliberately used for potential microwave assisted magnetic recording (MAMR) in digital data storage devices but can also unintention-

ally occur when working with microwave control fields for an NV close to the mu-metal structures of a HDD.

#### 2.4 MAGNETIC DOMAINS

Magnetic domains exist in a ferromagnetic material as a way to minimize its internal energy. In this case both direction and amplitude of the magnetization within the crystal is constant only within well defined domains of different size (see Figure 4 b). The diameters of magnetic domains can range from tens of micrometers up to several millimeters.

If an external magnetic field is applied the crystal reacts to this perturbation only by moving the borders of the domains. Domains whose magnetization is orientated in the same direction as the external field increase in volume whereas the volume of all other domains decrease. Only if the applied external magnetic field is high enough the magnetization of the whole crystal is oriented parallel to the field.

This description for ferromagnetic materials holds only for monocrystals. However ferromagnetic materials are usually polycrystalline. They are composed of microscopic crystalline grains, each holding a single ferromagnetic monocrystal with arbitrary lattice orientation. Usually the size of each grain allows to have multiple domains within a single grain (see Figure 4 c).

For some materials the grain diameter can be on the order of nanometers and therefore much smaller than the typical size of a magnetic domain. Then each grain is composed of only a single magnetic domain. Due to the arbitrary orientation of each grain's crystal lattice, the magnetization of adjacent grains points in different directions. The grain size is important for recording platters of HDDs as it gives a lower limit for the minimum physical size of a bit.

For most experiments the setup is a standard confocal microscope at room temperature for bulk diamond samples. It is extended by a HDD write head that is attached to an additional piezo stage. The write head lies onto the diamond's top surface and can be positioned independently of the microscope objective.

#### 3.1 OBJECTIVE AND HARD DISK HEAD SCAN

In Figure 5 (a) the diamond sample (1) and surrounding parts are depicted. The used diamond membranes have a thickness from 30  $\mu$ m to 50  $\mu$ m with implanted NVs 5 nm to 20 nm below the upper surface. An immersion oil objective (2) with a numerical aperture (NA) of 1.35 focuses green laser light (520 nm) to an diffraction limited spot inside the sample through the diamond's bottom side.

The objective is attached to a piezo stage allowing three dimensional scans. The PL is guided through a 635 nm longpass to filter out laser reflections, background and the {textscRaman line and subsequently detected by a single avalanche photodiode (APD).

Figure 5 (b) shows a two-dimensional scan of the microscope objective. The bright spots correspond to diffraction limited images of individual NVs.

The horizontal features stem from PL emitting components of the HDD head. The air-bearing surface (ABS) of the write head lies parallel in close contact on the upper surface of the diamond (see label (4) in Figure 5 a). The actual distance between ABS and diamond depends on the cleanliness of both surfaces. With optimal conditions separation between the surfaces as small as a few tens of nm can be achieved.

The HDD head is attached to a second piezo stage and can be moved independently of the microscope objective. Figure 5 (c) shows a PL scan of the writer with a fixed objective position. The scan shows similar writer features compared to the objective scan except the expected absence of NVs.

### 3.2 SPIN INITIALIZATION, READ-OUT AND CONTROL

The initialization and read-out of the NV's spin state is achieved optically, whereas microwave radiation is used for the spin control.

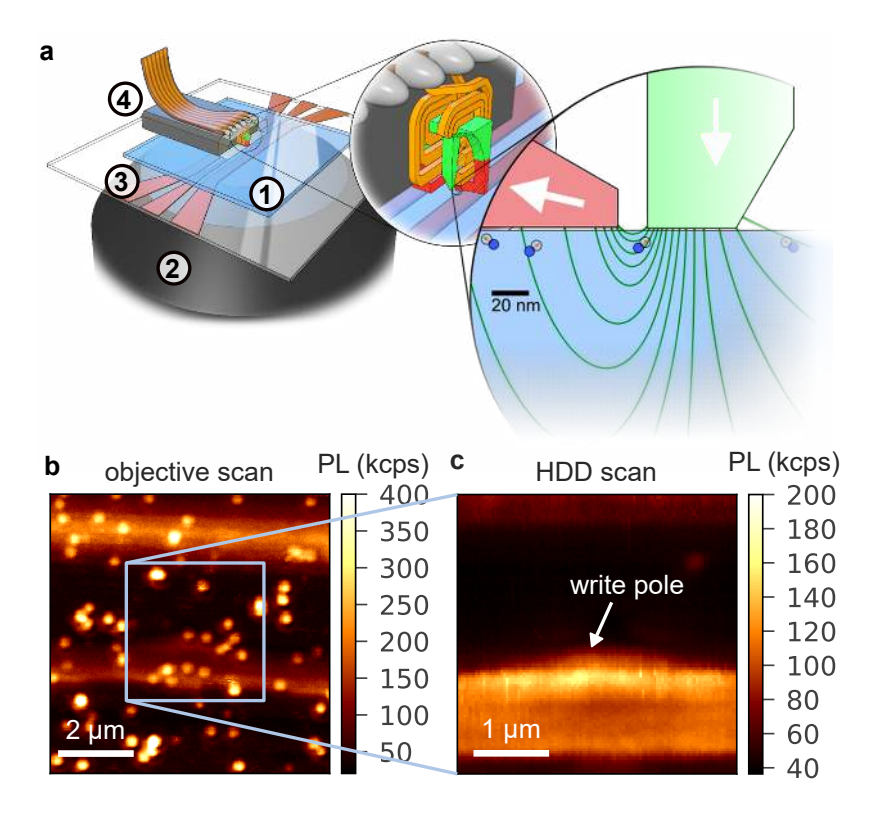


Figure 5: Setup and the two different scanning methods. **a**, schematic image of the setup (from [23]). The diamond sample (1) lies on top of a glass cover slide. The optical access is realized by a confocal microscope oil objective (2) (NA = 1.35) attached to a piezo stage. A copper wire (3) lies close to the sample to emit microwave control fields. The HDD head (4) lies onto the diamond sample and can be positioned by a second piezo stage. **b**, confocal scan of the microscope objective with fixed HDD. **c**, confocal scan of the HDD with fixed microscope objective.

The microwave radiation is emitted by a copper wire (label (3) in Figure 5 a) lying close to the sample and the HDD. This allows the coherent control of most of the NVs inside the sample.

If static magnetic fields are needed, a neodymium magnet is attached near the sample. Moreover, the writer can be used to create static as well as oscillating fields by applying direct currents (DCs) and ACs.

## 3.3 SAMPLES

The diamonds used in this experiment are type IIa chemical vapor deposition (CVD) layer. For most of the experiments a sample with a (111) surface orientation is used. Although (100) crystals are more common, it is sometimes advantageous to have one of the four NV orientations perpendicular to the diamond's surface. If an external magnetic field is perpendicular to the surface, as it is for perpendicular

magnetic recording (PMR) writers [31], it can be aligned to the NV axis. This has several advantages for initializing and read out.

The NVs are implanted into a roughly 10 nm deep layer of the diamond. For most experiments 99.99 % isotopically enriched  $^{12}$ C samples are used. Few measurements are also taken on more common samples with a natural abundance (about 1.1 %) of the carbon isotope  $^{13}$ C.

For the experiments described in the last part NDs with a maximum diameter of 50 nm are used. NDs are usually produced by milling bulk diamond samples. The resulting crystal fragments are more afflicted with lattice defect than bulk diamond. Also the distance between NVs and diamond surface has a high dispersion. These effects lead in general to shorter coherence times, worse charge state stability and more strain at the NV position compared to bulk diamond samples. Also the NV properties can differ heavily for different NDs.

#### 3.4 MODIFICATIONS FOR NANODIAMONDS

When looking at NDs with an oil objective they are likely dissolving in the oil. An alternative is attaching them upon a cover slide and use the slide's back side for the optical access. However, if the NDs should lie on a nontransparent substrate like the ABS of an HDD head on has to give up the oil. While looking at NDs the oil objective therefore is replaced by an air microscope objective with the drawback of a lower resolution.

In the relevant experiments the NDs are attached directly to the ABS replacing the bulk diamond sample in Figure 5 (a). The initialization, read-out or manipulation processes are unmodified.

#### 3.5 HARD DISC HEADS

For the experiments mainly three write head models are used. The conventional hard disk head experiments in Part ii are mainly realized with state-of-the-art Seagate write heads, like they are implemented in commercially available conventional HDDs. Other heads are provided by Integrated Solutions International but of unknown further origin.

The prototype heat assisted magnetic recording (HAMR) heads used for the experiments in Part iii are provided by SEAGATE too.

# Part II CONVENTIONAL HARD DISK HEAD

# FUNCTIONAL PRINCIPLE OF CONVENTIONAL HARD DISK DRIVES

To satisfy the expected exponential increase in demand for digital storage (see Figure 6 a) HDDs are the first choice for cloud applications due to their superior price per storage ratio. To further increase the device's capacity the relevant components have to be further miniaturized. For a research and development (R&D) department sensors able to investigate their properties on the nanoscale are of large interest.

Electron spin systems like the NV center in diamond can be used to characterize state-of-the-art HDD components. On the other hand HDDs are also useful for scientific applications unrelated to digital data storage technology. Thus, HDD components can be used as tools to manipulate spin system by taking advantage of their extraordinary combination of properties [23].

#### 4.1 STRUCTURE OF A CONVENTIONAL HARD DISK DRIVE

Commercially available HDDs heads (Figure 6 b) use magnetic effects to store digital information. Figure 6 (c)-(f) sketches the size ratios of characteristic HDD's components. HDDs use rotating ferromagnetic coated disk as the recording medium (c). The head gimbal assembly (HGA) (d) is attached to an actuator able to adjust the position of the read and write head (black box).

The HGA positions the head parallel to the recording medium in close contact. The head's bottom surface, the air-bearing surface (ABS), has aerodynamic features to control the airflow created by the disc's high rotation speed. By exploiting the aerodynamic ground effect the write head is flying with a distance of about 10 nm above the recording medium.

The actual writer is a lithographed microstructure integrated into the head. It consists of a pair of coils wrapped around a nickel-alloy core (e), that form the write and return poles perpendicular to the ABS. The write pole itself is an approximately 100 nm sized tip on the ABS, while the return poles end in large shielding brackets. The write and return pole are separated by a roughly 20 nm large gap, that defines the physical size and position of the bit.

When a current is applied through the coils it magnetizes the poles. Due to the geometry the magnetized poles create a strong magnetic field localized at the write pole (f). The magnetic field is locally larger than the coercivity of the recording medium and therefore able to

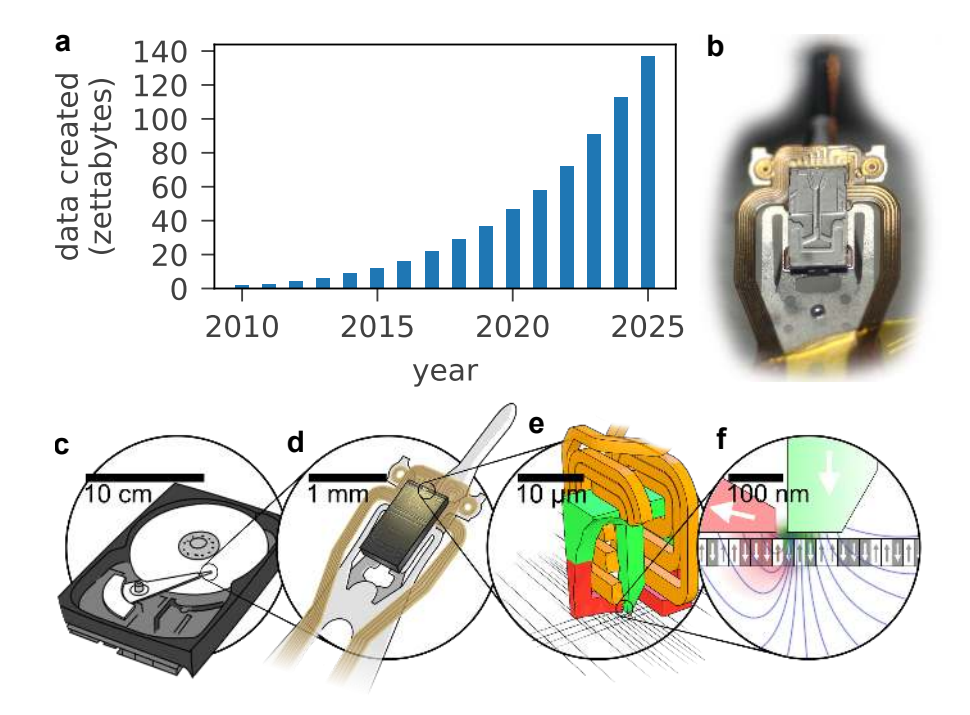


Figure 6: Overview about HDD technology. **a**, predicted amount of created data worldwide (from [32]). **b**, picture of an HDD head. **c**, commercial HDD with ferromagnetic recording medium and the HGA. **d**, HGA with the actual writer integrated in the head (black box). **e**, writer consisting of a pair of coils wrapped around a nickel-alloy core. **f**, localized and strong magnetic field produced by the write pole is able to flip the magnetization of a small ferromagnetic domain on the recording medium.

switch its magnetization. The digital information is then saved in the remanence magnetization of this domain.

### 4.2 THE WRITE FIELD

The poles geometry defines the spatial strength and orientation of the write field. Figure 7 shows FEM simulations for the field strength 10 nm (a) and 60 nm below the write pole. It is designed to have the maximum field strength (about 1 T) concentrated at the write pole. A high field gradient of up to 20 mT nm<sup>-1</sup> causes the field to drop drastically with rising distance to the write pole. As a consequence the area, where the write field is large enough to flip the magnetization, is limited to 20 nm. It is defined by the size of the gap between the write and return pole.

Typical HDDs flip the magnetization of a bit within a few nanoseconds. With a typical diameter of 3.5 Inches and a rotating speed with several thousand rotations per minute (rpm) this leads to a bandwidth on the order of gigahertz [34].

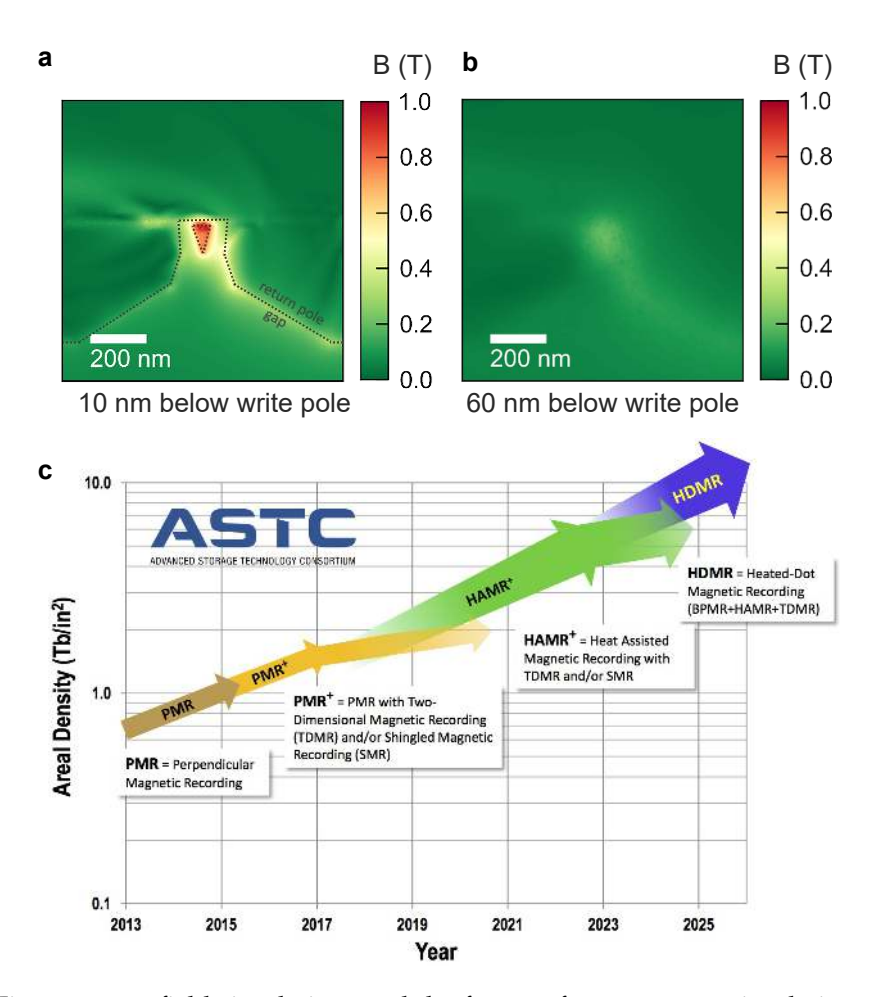


Figure 7: FEM field simulations and the future of HDDs. a, FEM simulation of the magnetic field of a conventional HDD head in a plane 10 nm below the write pole (from [23]). b, same as (a) but with a 60 nm distance. c, ASTC technology roadmap (from [33]).

The write field of state of the art HDD heads is perpendicular to the surface of the recording medium during the write process (see Figure 6 f). This process is denoted as perpendicular magnetic recording (PMR) [31] as mentioned above. To increase the storage density typically the localization of the write field is increased by miniaturization of the writer. However, for state-of-art HDDs the size of the magnetic domains is a limiting factor, too. The most promising approaches to overcome these limitations are microwave assisted magnetic recording (MAMR) [35] and heat assisted magnetic recording (HAMR) [36] (see Chapter 8).

Figure 6 (g) depicts a proposed roadmap for the future technology of HDD devices. Since the year 2015 state-of-the-art HDDs use PMR combined with a technique called shingled magnetic recording (SMR) whereby adjacent magnetic tracks slightly overlap to increase the storage density. For two-dimensional magnetic recording (TDMR) the concept of individual magnetic tracks is lifted even more. The roadmap predicts the rollout of HAMR devices in the year 2019. A further in-

crease of storage density could be possibly achieved by using bit patterned magnetic recording (BPMR). Instead of using a continuous magnetic film as the recording medium BPMR uses lithographed magnetic islands to store the digital information.

#### 4.3 BEYOND DATA STORAGE

The ability to control high magnetic fields focused on a nanometer length scale with a GHz bandwidth is crucial for the selective and coherent control of single electron or nuclear spins. Therefore an HDD's writer is a promising tool for the manipulation of spin-systems like the NV center in diamond. Due to the decades of developing effort it has a unique combination of properties, that is not simple to achieve with standard tools, like wires, permanent magnets or magnetized atomic force microscope (AFM) tips.

The high bandwidth allows to use the writer itself as a microwave antenna or to switch the field on and off on faster timescales than the typical relaxation of NV spin and hence within pulse measurement sequences. The high field amplitude allows to get easily into NV's high field regime. Finally, the high gradient opens up possibilities for addressing NVs spectrally by their individual Zeeman splitting.

This is not the first scientific work that covers the use of an HDD head in combination with an NV. In [23] several fundamental results were presented. In this chapter the relevant insights and methods of this publication are listed. They are the base for most of the experiments in this thesis.

The results showed that the NV is in principle a suitable magnetometer for the characterization of HDD writers and write fields can be used to control the full spin state, i. e. populations and coherences of both individual nuclear as well as electron spins.

#### 5.1 PHOTO LUMINESCENCE IMAGING

The NV's PL depends on the magnetic field. It can therefore be used to image magnetic features of the write pole's field. The challenge here is to separate the NV's PL from the PL of the head itself. In [23] the separation is achieved by using the different lifetimes of each emitter. Lifetime separation leads to a very low count rate, that on the other hand leads to long recording times for a high-resolution image. Apart from that the scans are almost free from artifacts and independent of the remanence magnetization.

In this thesis a different approach is used to image the magnetic field features like it is described in the supplementary information of [23]. For each pixel in the scan the PL is measured with (see Figure 8 a) and without (b) an applied current at the writer. The relative difference in the PL counts are then interpreted as the magnetic field effect. Figure 8 (c) shows the result of such a scan. Due to the higher count rate the time per pixel is drastically reduced. The time needed to record a scan is therefore much shorter compared to the lifetime separated scans. On the other hand, the scan is prone to the remanence magnetic field that leads to additional image artifacts in the "off" scan (see strips on the left side of Figure 8 b). The relative PL difference at the artifacts therefore cannot be interpreted trivially as an effect of the writer.

## 5.2 SPIN MAGNETOMETRY

In [23] magnetic field measurements of the write field at aligned NVs by determining the electron Zeeman shift were performed. Magnetic fields up to 200 mT were measured with gradients up to 587 μT nm<sup>-1</sup>. As the measurements were limited to alignment spots only writer

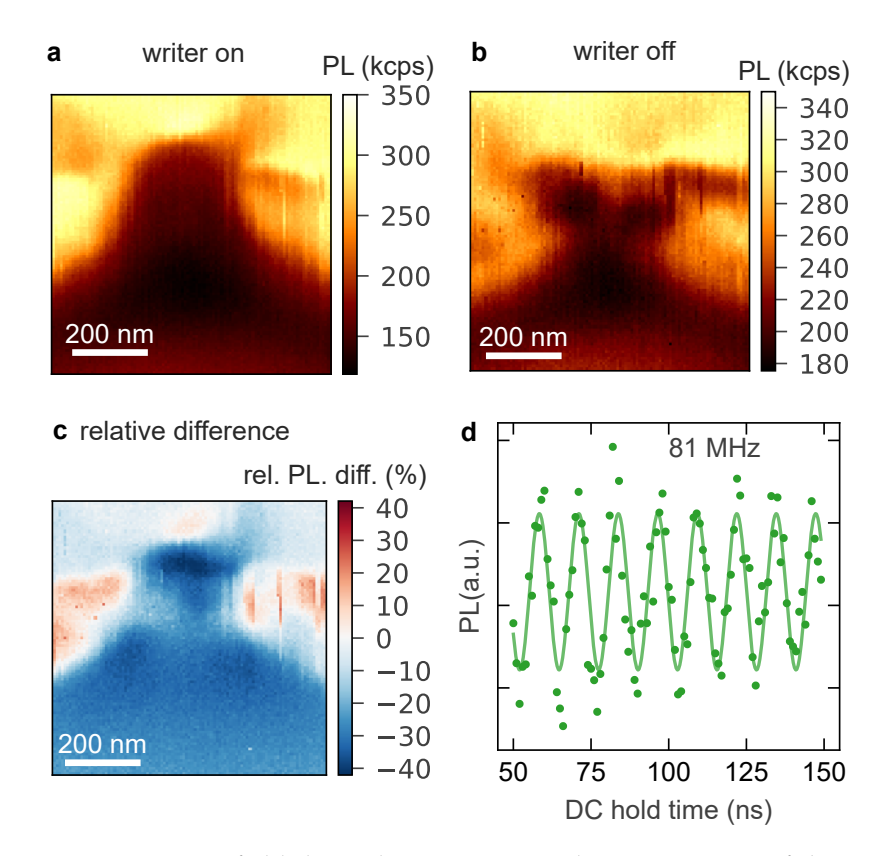


Figure 8: Magnetic field dependent PL scans and FID. **a**, PL scan of the HDD position while the writer is on. **b**, same as (a) but with no current applied at the writer. **c**, relative PL difference between (a) and (b). **d**, FID measurement with a write current during the evolution time.

regions with a magnetic field parallel to the NV-axis could be investigated. This prevented especially the recording of wide two dimensional magnetic field images. In this thesis this is solved (see Section 7.1) by pulsing the write field for the ODMR.

Furthermore the writer was used as a microwave emitting antenna. The maximum RABI frequency measured is 333 MHz. Also interference experiments were performed. As an example the result of a free induction decay experiment is shown in Figure 8 (d) whereby a current is applied at the writer during the evolution time resulting in a modulation of the spin precession by the applied magnetic field.

Not only the electron spin can be manipulated by the write field. In [23] a <sup>13</sup>C nuclear spin was driven resonantly with an AC field of the writer. While doing so a RABI oscillation for the nuclear spin with driving strengths up to 51 mT were realized.

Also a free induction decay experiment on the nuclear spin was performed. For an evolution time up to 2000 ns on the nuclear spin the signal shows a clear oscillation of 10 MHz. That corresponds to a static magnetic field level of about 40 mT.

#### PASSIVE OPERATION

The presence of the HDD's writer affects the NV even if it is passive, i.e. without applying a current. The relative position of NV and writer in combination with the NV's orientation has an effect not only on the amplitude of external control and static fields but also on the spin relaxation times.

## 6.1 WRITER POSITIONING

In the normal operation mode inside the HDD the head is flying close to the disc's surface without touching the recording medium. There the head can be positioned without friction by actuators and using the aerodynamic properties. The distance is actively controlled with the feedback obtained by a proximity sensor. For fine-tuning the writer has integrated heating devices, that can adapt the distance between ABS and recording medium with nanometer precision due to thermal expansion within a region close to the read and write components.

In contrast to this normal operation mode, in the scenario used for this thesis the head is in direct contact with the diamond's surface. The relative position between diamond surface and ABS is constant except for scanning measurements. Therefore friction between head and diamond cannot be avoided affecting the positioning accuracy on the nanoscale.

Furthermore, there is no active position stabilization due to the lack of accurate feedback. As the writer's structures are much smaller than the diffraction limit, optical feedback is not applicable. This makes the whole positioning process vulnerable to vibrations, thermal fluctuations and spontaneous release of stress at the HGA. In practice this leads to mismatches of two adjacent columns or rows in a two dimensional writer scan, drifts or spontaneous leaps in the writer's position during long- and short-term measurements.

On the other hand, this has the advantage that, once the setup is relaxed and in thermal equilibrium, external stress has to overcome static friction to move the head. The friction makes the head to stay at the same position for hours or days. This is a valuable feature for long-term, non-scanning measurements.

Figure 9 (a) shows a writer scan close to the write pole (2) of the relative PL difference as described in Section 5.1. The writer is mounted in such a way, that the shield structures should run horizontally. The diagonal features emerging in the figure at position (1) indicate unintended vertical drifts during the image recording.

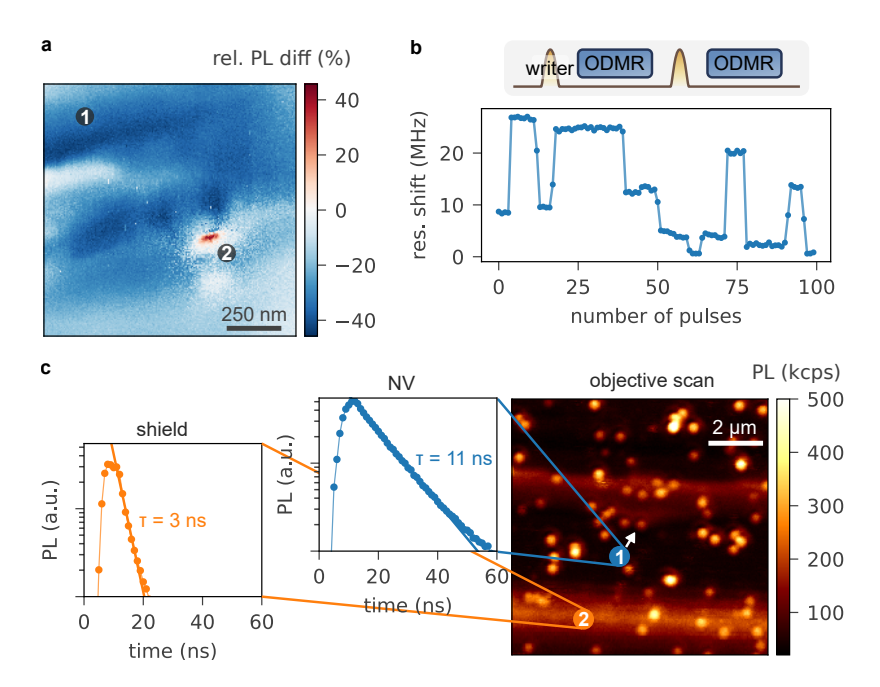


Figure 9: Basic operation of the writer. **a**, relative PL difference between applying a current and not applying a current at the writer. **b**, tracking of the remanence magnetization by measuring multiple ODMRs with write pulses in between. **c**, comparison of NV's and HDD's shield lifetime (confocal scan same as in Figure 5 c).

Since these drifts are not reproducible and do not occur for every scan, the scan process itself is often unreliable, as scanned features cannot be approached accurately. There is also the uncertainty that the scan is distorted in an unknown way.

## 6.2 REMANENCE MAGNETIZATION

The magnetic field of the writer is produced by a ferromagnetic lithographed pole based on a nickel-alloy. The pole's magnetization can be controlled by the current applied to the pair of coils (see Section 4.1). However, like an ordinary ferromagnetic material, the magnetization will not drop to zero when the current is turned off. Instead there remains a remanence magnetization.

Due to the geometry this can lead to quite large remanence fields at the pole that can be strong enough to significantly affect a close-by NV's behavior. As discussed in Section 1.4 transverse magnetic fields can especially influence the NV's PL if they are on the order of 20 mT.

The scan in Figure 9 (a) shows white and red features at the write pole. The colorbar is encoded in such a way, that a white color corresponds to an unchanged PL, if the current is applied at the writer or respectively turned off. As the writer's magnetic field in such a close distance to the pole should be sufficient to suppress the NV's PL this

is an indicator that the PL is already suppressed by the remanence field on the off image.

If the writer's field is aligned with the NV-axis, whereas the remanence field is not, the PL can be even increased when the writer is on. The red feature at position (2) in the scan can be described by this situation.

Strong remanence fields compromise the initialization and optical read-out of the NV and therefore the basis for many experiments. The search for spots, where the magnetic field is aligned to the NV-axis (alignment spot), can sometime solve this issue. For most of the scanning experiments the remanence magnetization is not avoidable and has to be taken into account.

Another issue regarding the remanence magnetization is depicted in Figure 9 (b). The measurement tracks the shift of one resonance line by applying ODMR measurements while the writer is off, with short pulses of the writer between each measurement. A shift in the resonance frequency is dominated by a shift in the magnetic field and therefore indicates variations in the remanence magnetization.

The curve features some plateaus, where the resonance remains constant for several write pulses. Between the plateaus huge jumps of several tens of MHz are identifiable. The instability of the remanence magnetization is also the source for the white speckles around the pole (position (2) in Figure 9 a).

One way to deal with this issue is to optimize the shape of the write pulses. Saturation, zero currents or inverted currents aggravate the shifts, whereas smoothing the pulse slopes leads to more stability. Degaussing pulses on the other hand, i.e. exponentially damped AC currents, exacerbate the behavior.

# 6.3 TIME RESOLVED PHOTO LUMINESCENCE RESPONSE

While reading out the NV's photo-luminescence one has to consider additional fluorescence features of the writer itself (see Figure 9 (c) right). In practice this is not a big issue as the writer's fluorescence is usually darker than a typical NV. In other words, it is unlikely to confuse or oversee an NV with a writer's feature. If it is nevertheless needed to separate both fluorescence signals, they can be distinguished and separated by their specific lifetime.

Figure 9 (c) shows two measurements for the lifetime of the PL signal. For the measurement a short 8 ns long laser pulse is used to initiate the PL. Subsequently the detected counts are plotted over the delay time at the detector. The lifetime of the NV is with 11 ns much longer than the lifetime of the signal emitted by the writer's shield (3 ns). This allows to count photons with a late arrival time and only observe the NV's signal.

## 6.4 DRIVE FIELD AMPLIFICATION

The Mu-metal structures integrated in the writer can be magnetized by external magnetic fields. The writer's geometry determines the field orientation close to the pole and is only slightly affected by the orientation of weak external magnetic fields. Therefore it is quite challenging to align external static magnetic fields to NVs close to the write pole.

The field amplification not only affects DC but also AC magnetic fields. This includes external microwave radiation used to manipulate the electron spin state. In this experiment the microwave control field is emitted by a  $50\,\Omega$  wire antenna with a constant output power in a distance of  $740\,\mu m$  in respect to the NV.

Without the head on top of the diamond surface this leads to Rabi frequencies of  $\Omega_{\rm ref,40~dB\,m}=500\,\rm kHz$  at a electric signal power of 40 dBm.

The passive amplification depends on the relative position between write pole and NV. In the scan of Figure 10 (a) the relative position is varied and the RABI frequency is measured for each data point with identical parameters. The amplification is particularly increased close to the write pole and the edges of the return pole.

If the write head is on top of the diamond, the microwave signal is passively enhanced by orders of magnitude. In this scenario no current is applied to the writer. The amplification of the signal can be monitored by measuring the Rabi frequency and comparing it to the wire-only situation. At a signal power of 20 dBm the highest observed Rabi frequency is  $\Omega_{\rm writer} = 35$  MHz.

The Rabi frequency  $\Omega$  is proportional to the driving field amplitude B, that is again proportional to the wire's current amplitude I. The current amplitude squared is on the other hand proportional to the AC driving signal power P. Altogether this leads to power

$$P \propto I^2 \propto B^2 \propto \Omega^2$$
 (8)

being proportional to the RABI frequency squared.

The signal power for the Rabi map is 20 dB higher compared to the reference measurement. A power difference of 20 dBm corresponds to a factor of 10 in the amplitude and Rabi frequency. Therefor the reference Rabi frequency at 20 dBm can be estimated as  $\Omega_{\rm ref}=50\,{\rm kHz}$  which is challenging to measure due to dephasing of the spin with the driving field.

Neglecting geometric aspects an estimation of the passive amplification of the field amplitude by the writer

$$\frac{B_{\text{writer}}}{B_{\text{ref}}} = \frac{\Omega_{\text{writer}}}{\Omega_{\text{ref}}} = \frac{35 \,\text{MHz}}{50 \,\text{kHz}} = 700 \tag{9}$$

can be made. Compared to the permeability of the mu-metal of about 80 000 to 100 000 [37] this is still quite small. This might be due to

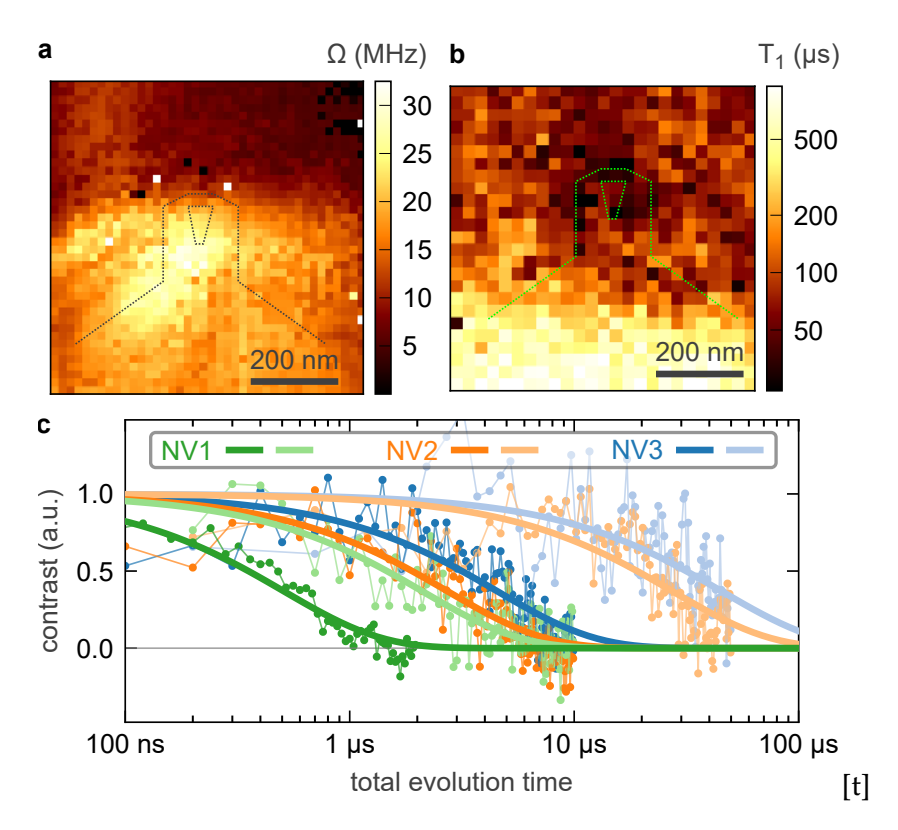


Figure 10: Passive applications of the writer. **a**, scan of the RABI frequency for a fixed driving current amplitude for different relative positions between write pole and NV. The dotted line outlines the shape and position of the write and return pole. **b**, similar to **a**, but T<sub>1</sub> measurement are done for each measurement point instead of a RABI measurement. **c**, comparison of T<sub>2</sub> times for three NVs (green, orange, blue) with (saturated) and without (pale) write head. The transverse relaxation times are measured by HAHN spin-echo protocols.

high frequency of microwave signal and could warrant investigation if there are not other bands with much larger amplification.

As the Rabi frequency depends not only on the amplitude of the driving microwave field but also on its polarization and the orientation of static magnetic fields, additional small features appear. The reason for the presence of static magnetic fields are the remanence field especially near the write pole. Due to the unknown geometric aspects in this scenario, the absolute amplification cannot be determined with certainty.

# 6.5 SPIN RELAXATION TIMES

The NV's longitudinal and transverse spin relaxation time give an upper limit for the timescale of a typical spin based measurement sequences. The longitudinal spin relaxation time  $T_1$  hereby describes how fast the longitudinal component of a spin decays into the ther-

mal equilibrium state (i. e. it describes the probability for spin-flips). On the other hand, the transverse relaxation times  $T_2$  describes the coherence of the system (i. e. the dephasing). For a single spin it describes the timescale for that a superposition state has a coherent phase evolution over time.

Relaxation destroys the system's information that is encoded in the spin state. If the information is stored in the population of states, the probability for random spin flips limits the storage time. On the other hand dephasing ruins information saved in the spin's phase. In other words the relaxation times limit the time duration during that the spin can be used for applications, be it to realize gates or save information for quantum information processing and communication or to interact with the environment for sensing.

Resonant field fluctuations or spontaneous emission are the origin for longitudinal relaxation. On the other, hand general field fluctuations shift the eigenenergies and lead to dephasing as well as coupling to spin baths.

The metal environment close to an NV affects its relaxation times and can be used for relaxometry measurements [38]. Many components of the writer are made of metallic materials and should therefore affect the NV's coherence times in the same way. Additionally, the antenna effect amplifies AC noise fields present in the noise spectrum. If they are in resonance with an electron spin state transition they can even affect the longitudinal coherence time.

For the map in Figure 10 (b) the longitudinal relaxation time  $T_1$  is recorded for each data point. To limit the runtime, the measurement is only 1 ms. For longer coherence times the evolution time has to be increased to achieve acceptable fit results.

The map shows relatively short longitudinal spin relaxation times below the return pole. The write pole reduces the relaxation times even more, indicated by the dark spot at the scan's center. At the bottom of the picture the coherence times are much longer due to absence of metallic structures. Typical T<sub>1</sub> times for this diamond sample without write head are on the order of several milliseconds.

Figure 10 (c) shows the writer's effect on the transverse coherence times  $T_2$ . The three colors (green, orange, blue) correspond to three individual NVs. Each curve represents a Hahn spin-echo measurement. The pale curves are measured without the write head for reference, whereas the saturated show  $T_2$  with the write head on top.

With the writer the  $T_2$  times for each NV are reduced by about an order of magnitude. The green curve with represents the usual situation with  $T_2$  times of only few hundreds of nanoseconds. However, for some configurations  $T_2$  times of a few microseconds (orange and blue curve) can be achieved. Long  $T_2$  times are crucial for interference or dynamically decoupling pulse sequences. The longest  $T_2$  time (blue curve) with the write head are on the order of  $3\,\mu s$ . Therefor basic

interferometric pulse sequences are applicable, but still quite challenging. However, measurement sequences requiring  $T_2$  times longer than a few microseconds are critical.

The transverse relaxation time is sensitive to dephasing induced by fluctuating magnetic fields. As magnetic field noise is as well amplified by the writer, the T<sub>2</sub> times are drastically reduced during the writer's presence. The T<sub>2</sub> times should also depend on the relative position between write head and NV. After trying several NVs at different position for distinct head models no pattern could be found.

Two dimensional  $T_2$  maps are not trivial due to the sensitivity of spin-echo measurements regarding pulse errors. As pulse errors occur quite often while working with the write head in scanning mode, an automated handling of these errors is quite challenging. By considering the long integration time needed for acceptable signal-to-noise ratio (SNR) the resolution of a  $T_2$  map is limited by the setup's long-term stability.

7

#### ADVANCED ACTIVE APPLICATIONS

In the previous chapter the writer is mostly used as a passive device. In this chapter the writer is operated actively. To control the writer's magnetic field it can be either connected to an arbitrary waveform generator (AWG) or directly to a microwave signal generator.

## 7.1 PULSED ODMR

High non-aligned magnetic fields affect not only the optical initialization process of the electron spin but also the spin state readout. This is the reason for the contrast of ODMR measurements being drastically reduced for high non-aligned fields greater than a few tens of mT [27].

With the writer's high bandwidth it is possible to separate the initialization and readout from finding the resonance frequency for a given magnetic field. The idea is to be at low field during these two critical parts, while doing the spin manipulation at a high static magnetic field level.

Figure 11 (a) shows a concept of a pulsed ODMR measurement, that is almost unlimited by field orientation or amplitude. Figure 11 (b) depicts the corresponding pulse sequences.

The pulse sequence initializes the electron spin state in the  $m_s=0$  state, while the writer is off (1). By ramping up the writer's current (2) a static magnetic field is established. If the following  $\pi$ -pulse is in resonance with the transition, one of the two other electron spin states is populated (green 3); otherwise nothing happens. For the readout, the writer's current is turned off (4). If the  $\pi$ -pulse was resonant, the electron spin is in the  $m_s=\pm 1$  state that results in a lower number of photons. If the  $\pi$ -pulse was not in resonance with the transition the electron is in the spin state with  $m_s=0$  and the NV shows bright luminescence.

To make this work the spin state has to follow the perturbation of the varying magnetic field in an adiabatic way. This is ensured by ramping relatively slow (200 ns ramp times) since faster variation of the magnetic field can lead to nonadiabatic transitions. Whereas this effect is undesirable for the pulsed ODMR scheme it is investigated and exploited in Section 7.5 to drive nonadiabatic fast passages.

Figure 11 (c) shows the result of such a measurement. With the two distinct resonances it is possible to derive the magnetic field |B| and alignment  $\theta$  (see Appendix A). For the data presented in the figure

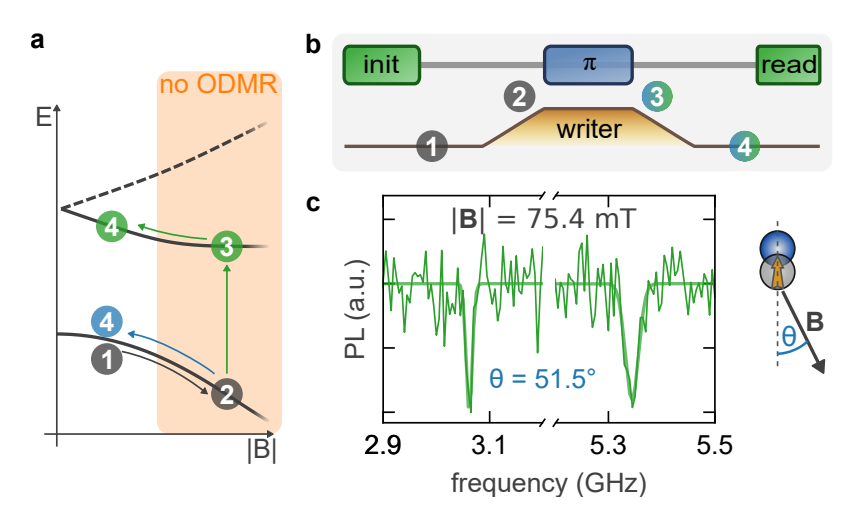


Figure 11: Measurement scheme for an almost field amplitude and orientation independent ODMR. **a**, energy level scheme with the state-positions during the sequence described in b. **b**, pulse sequence with the ramped write field. **c**, pulsed ODMR measurement for a field orientation of 51.5° and an absolute field strength of 75.4 mT.

the field amplitude is  $|B| = 75.4 \,\text{mT}$  and the field is misaligned by an angle of  $\theta = 51.5^{\circ}$ .

This measurement scheme is based on an initial population of the lowest eigenstate. For high magnetic field strengths the transition from the lowest to the highest state is forbidden since this would correspond to a transition between the  $m_s=\pm 1$  states (see Section 1.4). The spectrum would therefore reveal only one resonance. To be still able to derive the magnetic field the scheme has to be extended by e.g. additional pulses to populate the middle state.

# 7.2 MAGNETIC FIELD IMAGING

The pulsed ODMR technique described here, can also be used to do magnetic field imaging. To achieve an acceptable performance both a resonance tracking algorithm has to be developed and the location dependent transition rates have to be taken into account.

The latter issue can be addressed by using high and arbitrarily distributed power levels to achieve pulses with a large spectral bandwidth and to avoid pulse lengths of an even multiple of the  $\pi$ -pulse duration. The resulting pulses are not necessarily  $\pi$ -pulses. The disadvantage of a reduced contrast is on the other hand compensated by the ability to drive reliably transitions with an unknown RABI frequency.

Figure 12 shows the results of a magnetic field mapping approach. For each pixel the pulsed ODMR measurement sequence is applied. From the resonances the absolute magnetic field strength(a) as well as the transverse (b) and parallel (c) magnetic field component can be

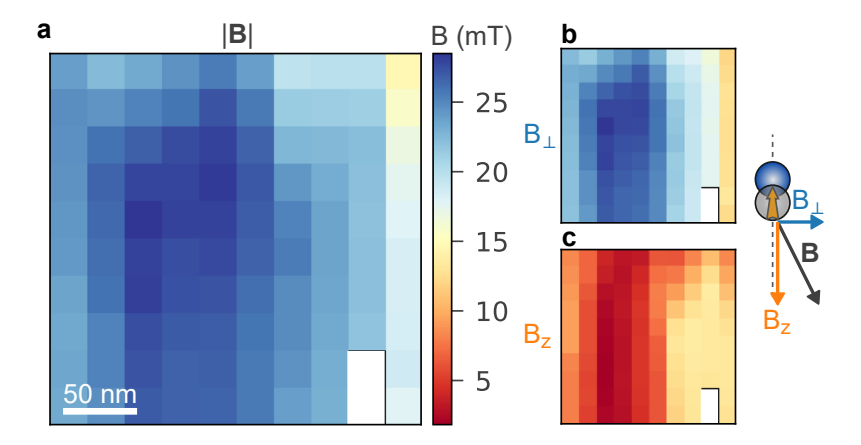


Figure 12: Magnetic field map. **a**, absolute value |B| of the magnetic field. For each pixel the pulsed ODMR measurement sequence is applied. The scan reveals magnetic field gradients up to  $50\,\mu\text{T}\,\text{nm}^{-1}$ . **b**, orthogonal component  $B_{\perp}$  of B in respect to the NV-axis. **c** parallel component  $B_z$  of B.

derived. Here field strengths up to  $27\,\text{mT}$  are achieved. These values are quite small compared to the maximum expected value of 1 T. The most likely reason is a larger distance between NV and writer than the working distance of 10 nm. From this measurement field gradients of up to  $50\,\mu\text{T}\,\text{nm}^{-1}$  can be derived.

The maximum expected magnetic field of the hard disc head is with 1 T about 30 times greater than the measured 27 mT. In a plain approximation it can be assumed the gradient to scale in the same way. Using the same factor of 30 this would lead to a maximum magnetic field gradient in the order 1 mT nm<sup>-1</sup>. This is in good accordance to the gradient measured in [23].

## 7.3 SPECTRAL ADDRESSING

A single NV can be aligned to one out of four different crystal axes. For each alignment there are two different orientations distinguishable by the order of the nitrogen atom and vacancy. Even though there are experiments that can identify the two orientations respectively [5] for most scenarios these two orientations are indistinguishable and therefore four effective configurations remain.

If there are more than four NVs in a confocal spot, at least two of them must have the same alignment. With a macroscopic magnetic field usually used for NV experiments, it is possible to separate the resonance lines for each NV due to their individual Zeeman shift except for those with the same orientation. Therefore it is not possible to separately drive, i. e. individually address, these spins with a microwave pulse.

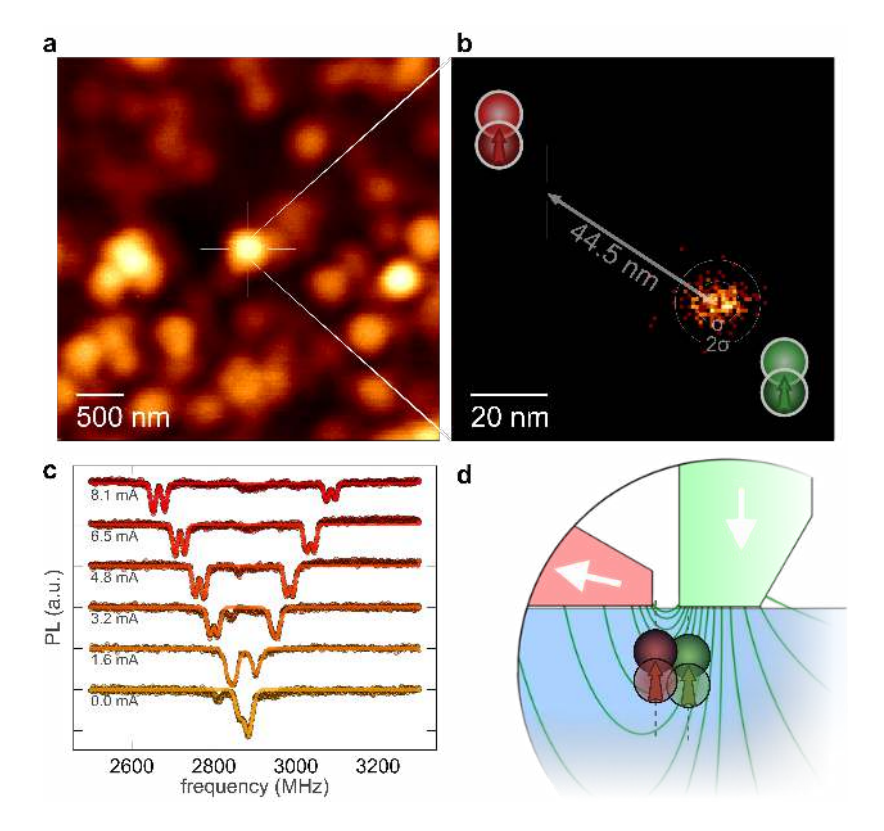


Figure 13: Spectral addressing of two [111] NVs. **a**, confocal scan showing NVs as diffraction limited spots. **b**, relative position between the two individual NVs. **c**, splitting of the resonance lines in dependence of the write field amplitude. **d**, schematic picture of the NV-pair write head configuration.

With a high gradient magnetic field it is possible to work with all NVs simultaneously no matter what the orientations are. Due to the slightly different positions, each NV is affected by an individual magnetic field strength and orientation [39]. This leads to an individual ZEEMAN shift of its resonance lines depending on the magnetic field and the crystal orientation.

The writer's high gradient is able to solve this addressing problem. In Figure 13 (a) a confocal image around a cluster of NVs containing two parallel [111] NVs.

To map the relative position (b) with super-resolution a modified version of deterministic emitter switch microscopy (DESM) [40] is applied. The idea is to do two scans whereby the brightness of the NVs is controlled individually by applying selective  $\pi$ -pulses. Whereas in [40] the two different scans are directly fitted here a two-dimensional convolution is applied first and fitted afterwards. Even if the information of the individual positions is lost in that way the accuracy of the relative position is distinctly increased, as the effect of collective drifts of both NVs is canceled out. The scan shown in Figure 13 (b) is a histogram of 500 individual measurements, showing a mean relative

distance of 44.5 nm and a standard deviation of 5.6 nm corresponding to a full width at half maximum (FWHM) of 13.2 nm.

Figure 13 (c) demonstrates the line splitting of two NVs with the same orientation ([111]). Each curve corresponds to one ODMR measurement whereas the writer current is increased from bottom to top. The high gradient leads to slightly different magnetic field at the NVs' positions (depicted in d) and therefore to a slightly different ZEEMAN shift. These different shifts and the corresponding option to selectively address the individual NVs make DESM for two parallel NVs possible in the first place.

For the topmost curve in (c) the magnetic field strengths are about  $7.93 \, \text{mT}$  and  $8.25 \, \text{mT}$  corresponding to a magnetic field gradient of  $7.1 \, \mu \text{T} \, \text{nm}^{-1}$ . The field is misaligned by an angle of  $16^{\circ}$  respectively  $27^{\circ}$ .

To classify the addressing abilities one can think about a quantum register array based on parallel dipolar coupled NVs [41]. Due to the hyperfine interaction with the nitrogen's nuclear spin an NV spectrum has a width of approximately 4 MHz. Therefore a splitting of the resonances for different NVs of 5 MHz to 10 MHz is desirable. With a spatial separation of about 20 nm a magnetic field difference of about 200  $\mu$ T to 400  $\mu$ T is needed (aligned fields assumed), leading to a magnetic field gradient greater than 10  $\mu$ T nm<sup>-1</sup>. The gradients of the hard disk head can be orders of magnitude larger and would present a suitable tool for the task.

#### 7.4 DRIVE FIELD ANTENNA

The writer's high bandwidth allows to apply AC currents at the transition frequency of 2.87 GHz like it was demonstrated in [23]. Therefore it is possible to drive RABI transitions with the magnetic field produced by the writer itself (see Figure 14 (a) left).

The Rabi frequency  $\Omega \propto B$  is proportional to the magnetic field amplitude of the driving field B. The exact relation between the electric current and the created magnetic field is not ascertained. In a basic approximation the dependence of the current on the magnetic field is assumed to be linear (B  $\propto$  I) similar to a macroscopic coil with a magnetic core.

Therefore the RABI frequency has a linear dependence on the applied current amplitude (right figure). The limitation factor for the maximum observed RABI frequency of about 300 MHz is not the current but the setup's timing resolution.

At lower frequencies the writer is expected to have less damping, i.e. the amplitude of an AC current driven microwave signal should be on the order of tens of millitesla. At low microwave intensities the transition between the  $m_s=1$  and  $m_s=-1$  is forbidden. For high intensities there is a low probability for a two-photon transition.

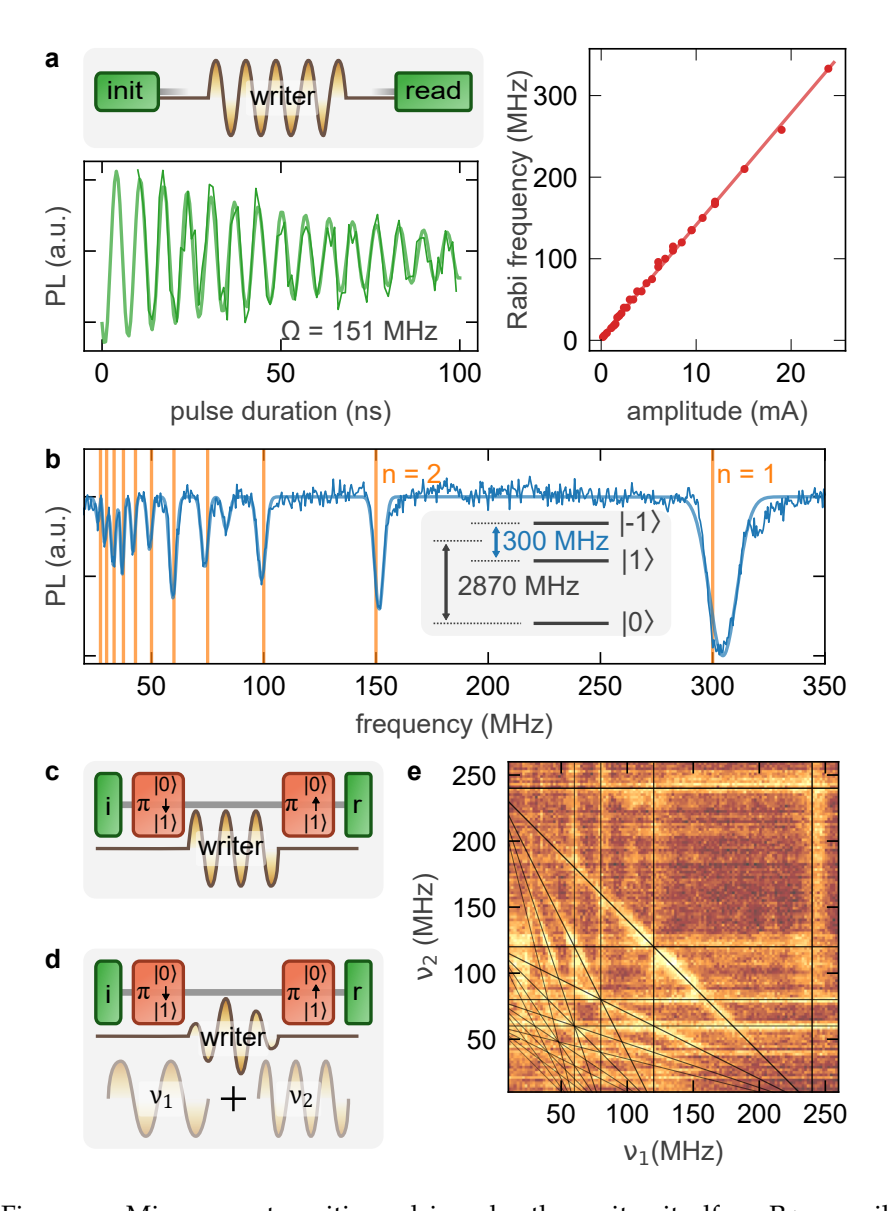


Figure 14: Microwave transitions driven by the writer itself. **a**, RABI oscillations (left) and power dependence (right) by applying an AC current at the writer. **b**, harmonics up to the eleventh order by driving the forbidden  $m_s=1 \rightarrow m_s=-1$  transition. **c**, pulse sequence for the harmonics ODMR measured in b. **d**, pulse sequence for the 2D-ODMR in e. **e**, 2D-ODMR with harmonics and sum-frequency generation.

Figure 14 (c) demonstrates the pulse sequence used to investigate these two-photon transitions. An aligned external permanent magnet splits the two  $m_s=\pm 1$  by 300 MHz. The green laser initializes the spin in the  $m_s=0$  state. Afterwards a resonant  $\pi$ -pulse populates the  $m_s=1$  state. By varying the frequency of the writer's AC current signal, the  $m_s=1 \rightarrow m_s=-1$  transition should be induced at a frequency matching half the resonance at 150 MHz. The population of the  $m_s=1$  state is then probed by a second  $\pi$ -pulse. A final green laser pulse reads out the population in the  $m_s=0$  state.

The spectrum shown in Figure 14 (b) indeed has a dip at 150 Mhz. Also the dip at the fundamental resonance frequency of 300 MHz can be explained by a slight misalignment of the magnetic field. Then the transition is not completely forbidden and the writer's high field amplitude is able to drive it.

Beyond these two dips several other features appear in the spectrum. Up to eleven dips can be identified that match almost perfectly to a harmonic series. Two theories can be used to describe the appearance of the other dips.

First, the higher harmonics can be multi-photon absorption processes. The second theory assumes a nonlinear response in the magnetic field to the initial sinusoidal current signal (see Appendix B). As the writer has ferromagnetic parts, that implies that the magnetic response should be nonlinear for sure, it could also be a combination of the two effects.

One should mention, that even without driving microwave transitions with the hard disk head often harmonics of the second or even third order appear in the spectrum due to nonlinear effects in one or multiple components of the microwave equipment. This spectrum's anomaly however is the appearance of the harmonics up to the eleventh order.

The pulse sequence described in Figure 14 d can be used to investigate nonlinear effects like sum-frequency generation. The writer's current signal is mixed by two different radio frequencies that can be varied independently. Figure 14 e shows the result of a 2D-ODMR measurement, that uses this kind of pulse sequence.

In addition to the harmonics (vertical and horizontal lines) also diagonal features are clearly visible. These correspond most likely to an effect called sum-frequency generation [42] that appears in nonlinear media. In this case two different frequencies add up and lead to a component in the spectrum of the sum of the initial signal frequencies. However, if the explanation of a nonlinear response or a multi-photon absorption is used, also the effect of difference-frequency generation should occur in the 2D-spectrum. These lines are missing.

The harmonic transitions can be driven in a coherent way. Figure 15 a shows a RABI oscillation of 4.7 MHz for the third harmonic at 151 MHz (fundamental at 450 MHz) with a signal power of -8.0 dBm.

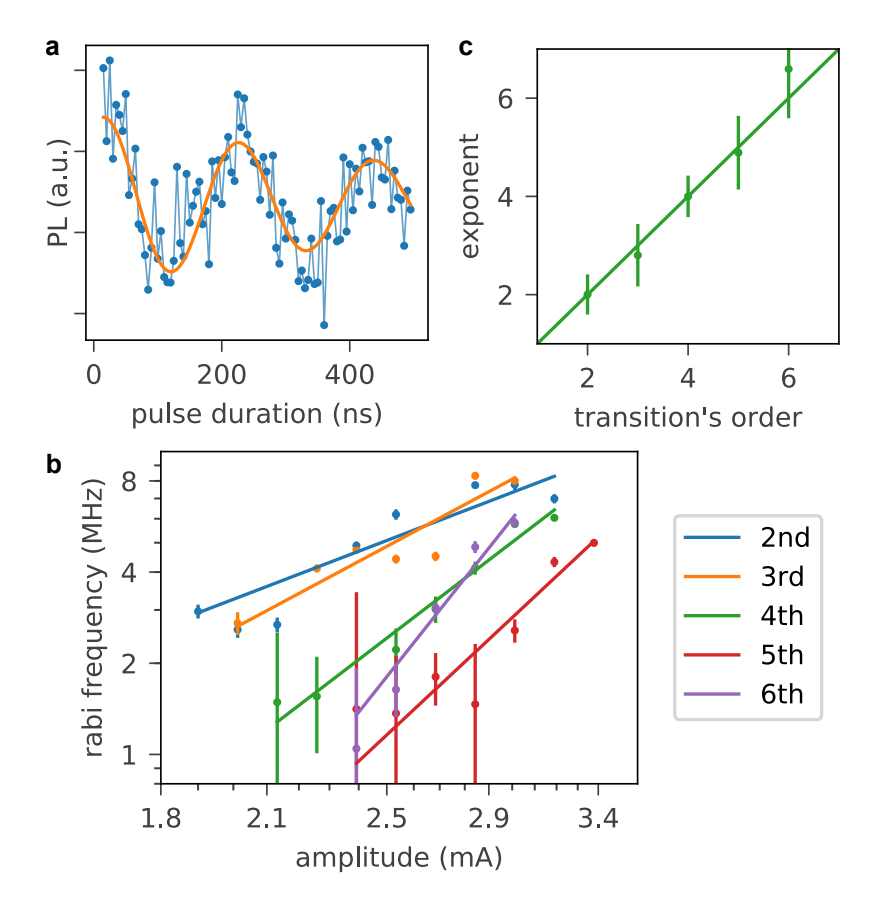


Figure 15: Coherent driving of the harmonic transitions. **a**, example Rabi of 4.7 MHz for the third harmonics at 150 MHz for –8.0 dBm signal power. **b**, power dependence for the Rabi frequency of the second to the sixth harmonic. **c**, power scaling of the Rabi frequencies for the transitions up to the sixth order. The Rabi frequencies are proportional to  $\rm I^c \propto B^c$  with an individual exponent c for each transition order.

Due to the signal's fast decay, only fast RABI frequencies greater than 1 MHz can be determined with acceptable precision.

Figure 15 b shows the result of an attempt to measure the power dependence of the Rabi frequencies for different harmonics (second to sixth order). It is expected that the second harmonic scales with the square of the magnetic field amplitude; the third scales with the cubic and so on. The results seem to confirm this theory, although the results have great uncertainties. The scaling with the power can also not be used to distinguish between a multi-photon absorption or a multi-harmonic generation process, as both effects have the same power-scaling.

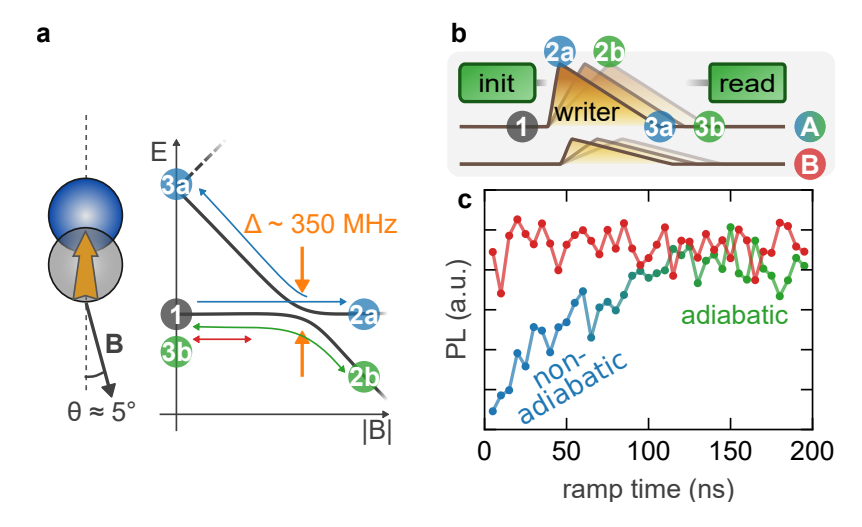


Figure 16: Landau-Zener transition. **a**, level scheme at the LAC. **b**, pulse sequence for the nonadiabatic fast passage. **c**, measurement result for this pulse sequence.

## 7.5 NONADIABATIC FAST PASSAGE

The high bandwidth of the writer in combination with the high field amplitudes allow to investigate adiabatic and nonadiabatic transitions of the electron spin state. For slightly misaligned magnetic fields (only a few degrees) there is a level-anti-crossing (LAC) between the initial  $m_s=-1$  and  $m_s=0$  state (see Figure 16 a).

For this experiment a diamond membrane with a surface parallel to the (111) crystal plane is used. In doing this it is ensured that there are NVs with their axis orthogonal to the surface. The magnetic field close to the write pole is assumed to point out of write head's surface. Then it's convenient to align the magnetic field directly underneath the pole where the field is the strongest. This results in an avoided crossing with an energy splitting of

$$\Delta E_{LAC} = \sqrt{2} \gamma_e B_{\perp} \ . \tag{10}$$

In the experiment the field is misaligned by about  $\theta=5^{\circ}$ . This leads to magnetic field components of  $B_z=102\,\text{mT}$  and  $B_{\perp}=8.9\,\text{mT}$  at the LAC that corresponds to an energy splitting of  $\Delta E_{LAC}=h\cdot350\,\text{MHz}$ .

The pulse sequence in Figure 16 (b) can be used to investigate nonadiabatic fast passages with the configuration described above. The electron spin is initialized in the  $m_{\rm s}=0$  state. Then the magnetic field is ramped up with a varying ramping time. For the readout the writers field is ramped down slowly.

Depending on the ramping time the electron spin either does an adiabatic transition (long ramp times, green curve) or a nonadiabatic fast passage (short ramp time, blue curve). For the red curve in Fig-

ure 16 (c) the ramp amplitude is reduced to not reach the LAC and can be seen as a reference measurement.

The transition probability in dependence of the ramp time can be described by the Landau-Zener-formula [43]

$$P_{LZ} = e^{-\frac{\pi}{2}\frac{\Delta^2}{\hat{v}}} . \tag{11}$$

Here,  $P_{LZ}$  is the transition probability,  $\Delta = \sqrt{2}\gamma_e B_\perp$  is the energy splitting at the LAC with the gyromagnetic ratio  $\gamma_e$  and the perpendicular magnetic field component  $B_\perp$ .

The energy change  $\dot{\nu}=g\mu_B\dot{B}$  determines the kind of transition. If  $\dot{\nu}\ll\Delta^2$  the transition is adiabatic (green curve). If otherwise  $\dot{\nu}\gg\Delta^2$  the nonadiabatic transition is more likely.

The experiments demonstrate that it is in principle possible to flip the spin with fast ramps of the writer. The nonadiabatic fast passage should in theory be a coherent transition. However, we were not able to observe a coherent state to investigate the coherence.

A conceivable experiment could use an FID like measurement sequence, whereby the first  $\pi/2$ -pulse is replaced by a ramp up of the writer's current to create a superposition between the  $|m_s=0\rangle$  and  $|m_s=-1\rangle$  states. The current is held constant during the evolution time and is completed by a ramp down, that replaces the second  $\pi/2$ -pulse.

The superposition states should oscillate with the frequency of the energy splitting on the Bloch sphere. To investigate this oscillation the ramps and the magnetic field level during the evolution time have to be achieved in a more accurate and reproducible way.

# 7.6 OUTLOOK

The last chapters show the possibilities of implementing HDD's write heads in spin physics experiments. An improvement in the electronics could possibly reduce magnetic field fluctuations. Then HDD-NV constellations with extremely fast coherent gates on the order of 1 ns by using the fast nonadiabatic fast passage are imaginable.

For further experiments especially the high gradient can be useful. In Section 7.3 e.g. the addressing of individual NVs is demonstrated.

Beyond that it can also be used to image single nuclear spins on the nanoscale in three dimensions, that are not directly attached to an NV. In [18] a MRI-like approach of detecting dark electron spins with subnanometer spatial resolution is demonstrated using a magnetized AFM tip. An HDD writer could conceivably replace the AFM tip to create the necessary gradients.

The spatial resolution of imaging techniques based on MRI is proportional to the spin interrogation time and the target spin's gyromagnetic ratio. As gyromagnetic ratios for nuclear spins are orders of

magnitude smaller than for electron spins much longer spin interrogation times are necessary to achieve a comparable spatial resolution when using the same magnetic field gradient.

The gradient produced by hard disk writers (> 1 mT nm<sup>-1</sup> [23]) are on the same order of magnitude than gradients based on magnetized AFM tips (also > 1 mT nm<sup>-1</sup>) [18]. The advantage of HDD gradients is the capability of switching the gradient on and off within a nanosecond timescale.

For many spin manipulation experiments the remanence magnetization and the short coherence times are a limitation. As these properties differ for different write heads, trying more head versions even from older HDD generations could lead to an improvement of the hard disk head's properties that are relevant for spin experiments. One could finally also think about using the know-how needed to design HDD heads for microstructured devices specially optimized for spin physics experiments.

The capabilities for an NV based tool for an R&D department can be improved by using a diamond AFM setup [44]. Especially the challenges regarding the positioning of the NV sensor in respect to the ABS can then be bypassed. This would not only allow to reliably record two-dimensional magnetic field images but also to adjust the height of the NV above the ABS and therefore to record three-dimensional magnetic field maps.

# Part III HEAT ASSISTED MAGNETIC RECORDING

#### FUNCTIONAL PRINCIPLE OF HAMR DEVICES

To increase the storage density for conventional HDD devices not only the limitations in current fabrication methods for the writer have to be considered but also the fundamental limits of the grain size of the used recording media. The latter gives a lower bound for the minimum bit size as the digital information is saved in the remanence magnetization of the magnetic domain.

To overcome this limitation materials with higher coercivity and smaller grain size has to be used as the recording medium. This comes with the drawback that the magnetic field produced by the writer has to be stronger too, but still has to be focused to achieve smaller bit sizes. heat assisted magnetic recording (HAMR) [36] has the potential to deal with all of these challenges at once.

The results presented in this part of the thesis are obtained in collaboration with Seagate Technology PLC. They provided the prototype HAMR heads and gave instructions on how to operate them.

# 8.1 BASIC PRINCIPLE OF HEAT ASSISTED MAGNETIC RECORD-ING

The fundamental idea behind the HAMR technique is depicted in Figure 17 (a). To reduce the grain size a material with high coercivity is used as the recording medium. Instead of scaling up the writer's magnetic field the medium is heated up to reduce the coercivity in only a small volume. The digital bit can then be saved in the small region where the writer's field and the heat spot overlap.

In practice this can be achieved by integrating a laser diode into the writer (see Figure 17 b). The laser light's electromagnetic energy is transferred by a waveguide structure to a small gold nanoantenna. The antenna transmits the energy to the recording medium by plasmonic near field enhancement.

Figure 17 (c) shows a photo of a prototype HAMR head. The infrared light (rendered violet by the camera) is emitted by the integrated laser diode operating at about 800 nm. Although the prototypes work in principle, they lack long term reliability. The limiting component here is the thermal stability of the gold nanoparticle. Therefore it is interesting to investigate sensors that can map the temperature on the nanoscale. In the next chapters it is tested and discussed, whether the NV as a single spin solid state sensor is suitable for this application.

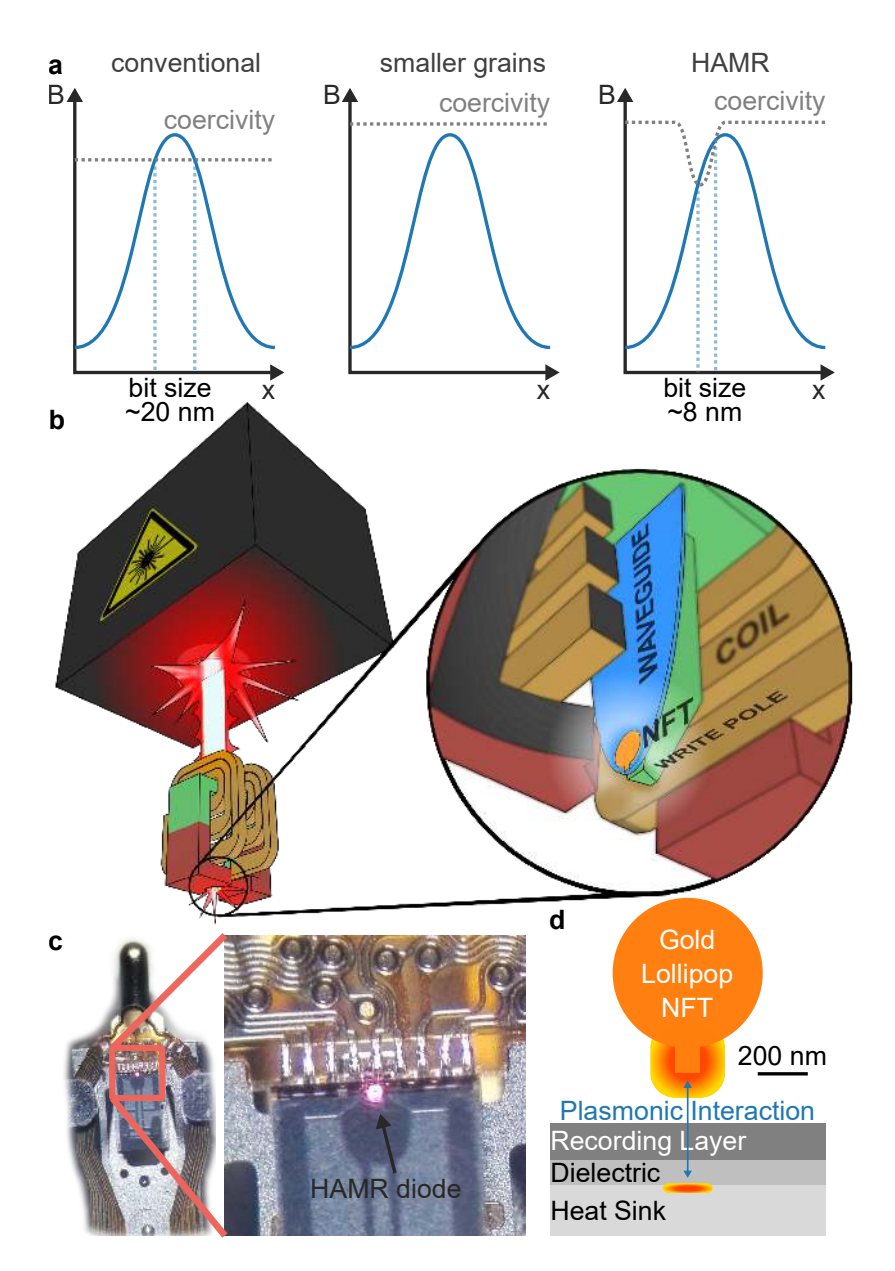


Figure 17: Basic working principle of a HAMR device. **a**, the coercivity is increased to reduce the grain size. To write the bit a heat spot reduces the coercivity in a small volume overlapping with the write field. **b**, schematic picture of the HAMR write head. The laser diode couples electromagnetic energy into a waveguide that transports it to an NFT made of gold. **c**, photo of a prototype HAMR head. The violet light comes from the integrated laser diode. **d**, schematic picture of lollipop, recoding layer, dielectric layer and heat sink.

#### 8.2 NEAR FIELD TRANSDUCER

To realize the idea of HAMR devices electromagnetic energy has to be efficiently coupled to the recording medium confined to a spot much smaller than the diffraction limit. With conventional far-field optics the minimum spot size is diffraction limited and on the order of the wavelength.

Near-field effects of plasmonic structures, however, are not constrained to this limit. Plasmons in general are the quantized collective oscillation of an electron plasma. At the interface between a metal and a dielectric medium they can be excited as surface plasmons (SPs). SPs have the advantage that they are both localized to the interface's surface but can also couple efficiently to external light. If the external light field is in resonance to an SP the light field close to the surface can be orders of magnitude greater than the original excitation field. This effect is called near field enhancement.

For plasmonic applications gold is very popular as it has both good chemical and thermal stability. Due to gold's interband transitions the wavelengths have to be higher than 700 nm.

To localize SP an antenna design as depicted in Figure 17 (d) can be used. The lollipop like shape is built up of a disc and small peg at its bottom. The surface plasmons excited in the gold lollipop can couple efficiently to surface plasmons on the interface between copper layer and the dielectricum by taking advantage of the lightning rod effect. A setup like this is called a near field transducer (NFT). The copper layer here acts as a heat sink as well as an image plane for the electric field.

The electric field is not only enhanced at the positions of the SPs but also in the volume between in the recording layer. Whereas the recording layer itself is not plasmonically active, the enhanced electric field can heat it up and therefore decreases the coercivity in that way. With the lower coercivity the magnetic field of the writer can flip the magnetization in its overlap.

Since the physical bit size is defined by the overlap and not only by the magnetic field gradient, less requirements must be fulfilled by the write field compared to conventional HDD writers.

9

#### AIRBRUSHED NANODIAMONDS

The basic functionality of HAMR devices is well understood and first prototypes are promising [45]. However, most of them lack long-term stability and withstand intensive usage over a much shorter time period compared to conventional HDDs. The most critical components of HAMR heads are not the laser diode or optic components but the gold lollipop revealing thermal instabilities after a large amount of write cycles.

Theoretical simulations predict temperatures of the gold lollipop up to several hundred degrees Celsius. For the development of more persistent NFTs nanoscale sensors able to measure these temperatures are desirable. NVs within nano- or nanostructured diamonds are potential candidates for this kind of nanoscale temperature measurement and a potential alternative for scanning thermal microscopes (SThMs) based on electric conductivity.

Since diamond is a material with one of the best thermal conductivity bulk samples cannot be used to measure temperatures on the nanoscale due to heat dissipation. The challenge of heat dissipation is also important for diamond nanopillars [46] in the non-contact operation mode (see Section 9.2). Therefore for the first studies presented in this thesis NDs are used. Their small volume can be heated up efficiently without dissipating the heat to a large thermal bath. Section 9.3 describes conventional methods of attaching nanodiamonds in a certain density on a surface. Section 9.4 explains a new method that is more suitable for profiled surfaces like the ABS of the HAMR heads.

### 9.1 TEMPERATURE MEASUREMENT OF THE GOLD LOLLIPOP

The NV can be used as a temperature sensor by exploiting the temperature dependence of the ZFS (see Section 1.5). Most temperature measurement schemes for single NVs require an aligned or zero magnetic field for absolute temperature measurement. As the writer with its ferromagnetic components is close to the lollipop an alignment or compensation of its magnetic field is not an option.

Therefore the presence of an unknown magnetic field close to the lollipop cannot be avoided trivially. A single ODMR measurement gives not enough information to determine all uncertainties like magnetic field strength and orientation or crystal strain and ZFS to determine the temperature. This is why absolute temperature measurements at the lollipop are quite challenging.

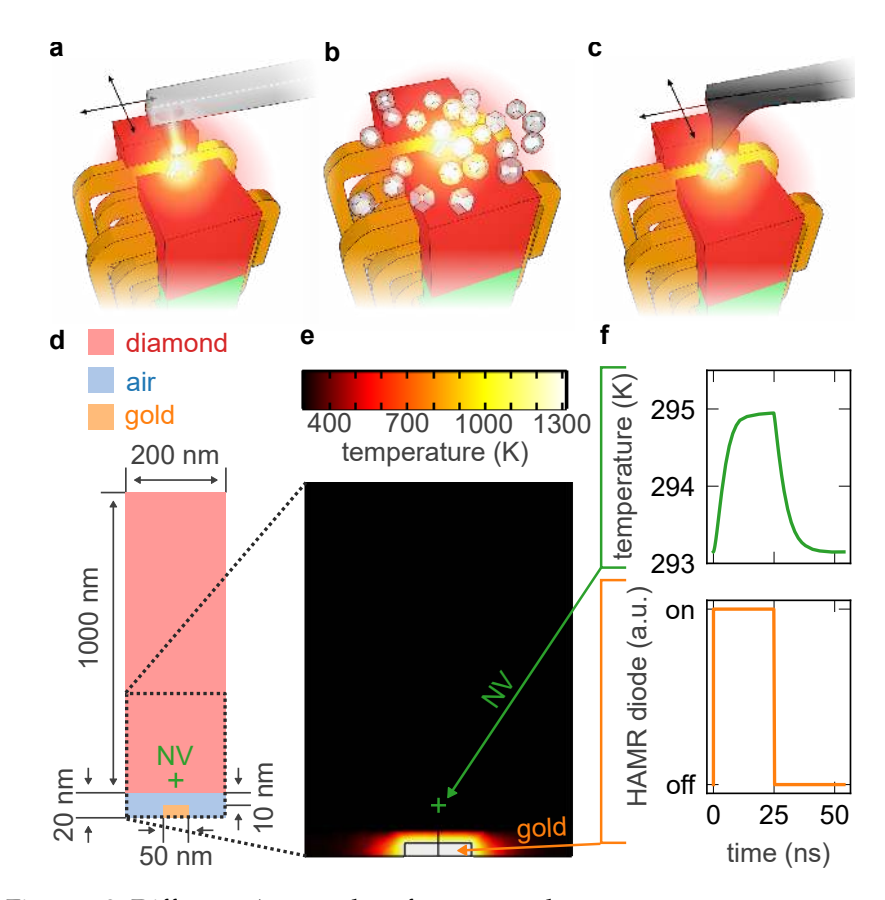


Figure 18: Different Approaches for nanoscale temperature measurement. **a**, scanning diamond nanopillar. **b**, arbitrarily distributed nanodiamonds. **c**, scanning pillar with attached nanodiamond. **d**, schematic outline of the model used for the temperature simulation in (e). **e**, 2D temperature simulation of a diamond nanopillar in the saturation regime. **f**, temporal simulation for the temperature at a 10 nm deep NV in the nanopillar.

However, relative temperature measurements should be feasible. By comparing the resonance position with and without operating the HAMR diode a temperature shift of up to tens of MHz corresponding to temperature shifts of hundreds of degrees Celsius would be expected and should be detectable. Under the assumption, that all other parameters stay constant, this should lead to at least an estimation for the relative temperature shift.

# 9.2 APPROACHES FOR A NANOSCALE TEMPERATURE MEASURE-MENT

Bulk diamonds are unsuitable for nanoscale temperature measurements due to the extraordinary thermal conductivity of diamond. The dimension of a diamond nanopillar [46] (see Figure 18 a) is much smaller, compared to bulk diamond samples. Typical pillars are of

almost cylindrically shape with a diameter of 100 nm and a length of 1000 nm. The NV is usually positioned in a depth of about 10 nm measured from the pillar's tip.

Nanopillars made of diamond are fragile. To prevent damaging them, it is much safer to operate them in non-contact mode with a distance of about 10 nm between the pillar's base and the sample. The 10 nm layer of air between the diamond and the HAMR head as the sample have to be considered for temperature measurements as well as the heat dissipation of the diamond pillar itself.

In Figure 18 (d) a 2D temperature profile of a system containing the pillar, a gold disc and a layer of air is simulated using COMSOL MULTIPHYSICS' simulation software. In the simulation the gold disc has a diameter of 50 nm with a height of 10 nm. The pillar is modeled as a 200 nm wide cylinder with a height of 2000 nm. The distance between pillar and gold disc is 10 nm. The remaining volume is modeled with air.

At the beginning the temperature of all components is set to room temperature (273.15 K). The HAMR diode is simulated by using the gold disc as a heat source.

Figure 18 (d) shows that the gold disc increases its temperature by approximately 1000 K. Whereas the air within a few nanometers around the disc is heated up, the nanopillar seems to be only negligibly affected. Detailed analysis indeed shows, that the temperature in a depth of 10 nm at the position of potential NVs is increased by only about 2 K. This makes the nanopillar in non-contact mode inappropriate for temperature mapping.

To analyze the dynamics of the system a step-like function for the diode is used (see Figure 18 e). The top graph shows the temperature at the NV position. The dynamics occur mainly in a 20 ns long time window. For longer heating or cool down processes the system saturates.

A much more promising approach for accurate temperature measurements is to use NDs distributed directly on the ABS instead of nanopillars (see Figure 18 b). In this way the problem of heat dissipation is solved. Also there is no gap between the ND and the ABS. This comes with the disadvantage that no scanning is possible. Additionally the positions of the NDs are typically coated on surfaces leaving them in random positions. Hence, to place one close to the NFT might require multiple attempts.

Figure 18 (c) depicts a theoretical approach that combines the advantages of NDs with scanning capabilities of a nanopillar is to attach an ND to the tip of an AFM. Since it is not trivial to attach an ND precisely on an AFM tip [4] the experiments are performed with dispersed NDs.

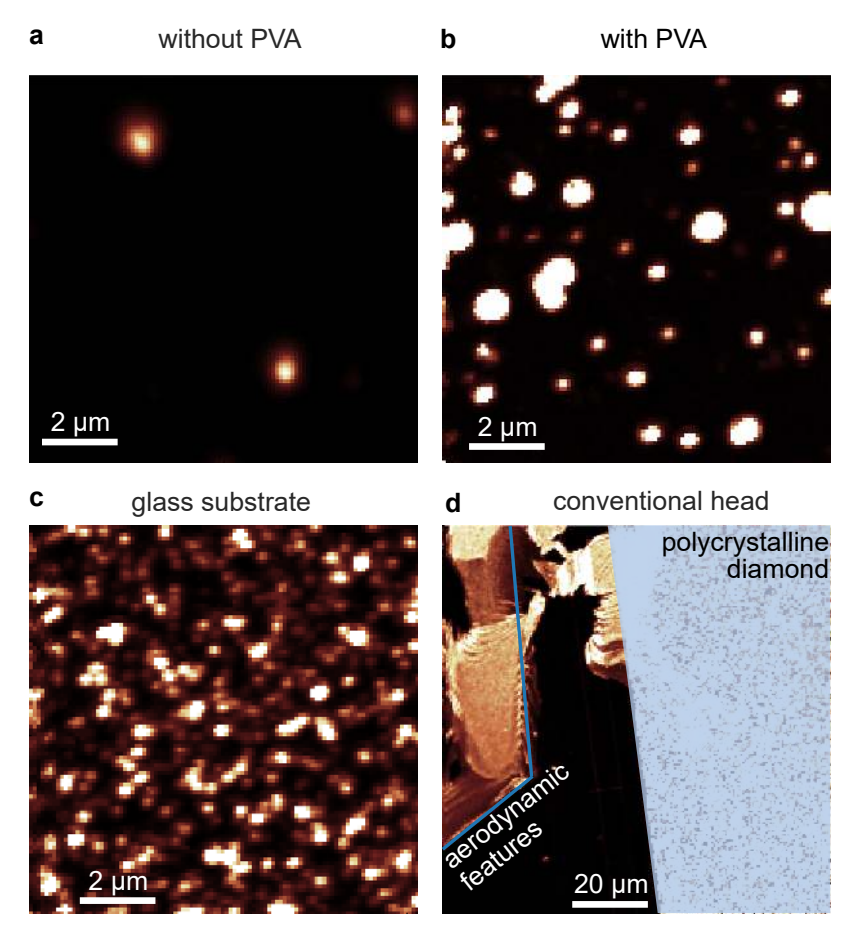


Figure 19: Confocal scans of spin coated NDs. **a**, spin coating without PVA. **b**, spin coating with subpar ND concentration. **c**, spin coating on a flat glass substrate. **d**, spin coating on a conventional HDD head. Due to the head's aerodynamic features (different materials with different surface properties) the distribution of NDs is far from being homogeneous.

# 9.3 SPIN COATING

Spin coating is the common technique to create thin films out of a liquid or solution on a flat substrate. The sample is attached to a rotating stage spinning up to several thousand rpm. A small amount of liquid is then applied to the substrate's center. Due to centrifugal force the coating material spreads out evenly on the whole substrate's surface.

To distribute NDs on a flat glass substrate spin coating can also be used. Figure 19 (a) shows a confocal scan of a cover slide spin coated with a colloid of NDs and water. Here the bright spots correspond to NVs in a cluster of caked NDs.

To separate individual NDs a solution 0.15% (w/v) polyvinyl alcohol (PVA) is used instead of pure water. The resulting contribution of NVs showed in Figure 19 (b) is much more homogeneous compared to

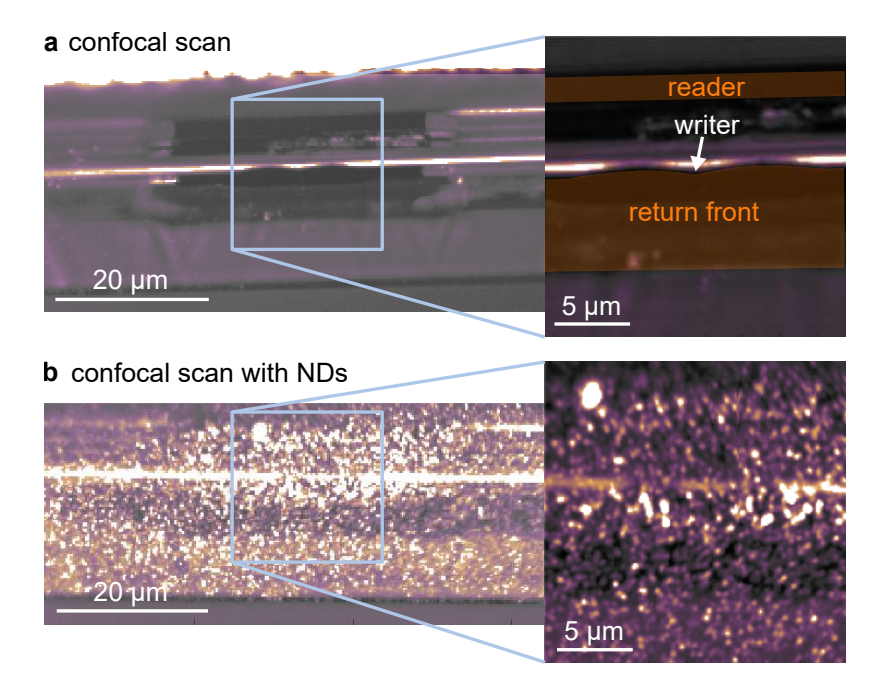


Figure 20: Confocal scans of a conventional HDD head. **a**, confocal scan of a cleaned head. The position of the writer can easily be localized due to PL features of surrounding components. **b**, confocal scan of an airbrushed head. The bright spots correspond to NVs in NDs. They are almost homogeneously distributed.

(a). By modifying the treatment of the solution and varying the concentration of NDs and spin coating parameters (time, speed, type of ramps) the NV density can be further optimized. Figure 19 (c) shows an almost ideal distribution of NVs. The density is a few NVs per 1 µm² while the spot's brightness indicates only a few NVs per spot. This is important because it is essential to observe the NDs that are in contact to the surface rather than the top layer of stacked NDs.

While spin coating works excellently for flat homogeneous substrates it fails dramatically when going to profiled and diverse surfaces like the ABS of an HDD head. Figure 19 (d) shows a confocal scan of a conventional head after it is spin coated with NDs. The result is far from a homogeneous distribution of NVs. Instead the NDs accumulate at aerodynamic features and overflow the structures at some positions. The sharp edge on the right side of the scan corresponds to the polycrystalline diamond structure integrated in the write head itself.

## 9.4 AIRBRUSHING

Due to the profiled structures of the ABS spin coating is not a suitable technique to get a homogeneous distribution of NDs close to the write pole. When thinking about alternatives, methods for creating

thin films of paint can be an inspiration. A promising technique is airbrush. By replacing the paint with a very dilute colloid of NDs this method can be used to homogeneously spray NDs even on rough surfaces.

When compressed air is guided through the airbrush pistol the Venturi effect leads to a locally reduction of the air pressure [47]. This brings the colloid (NDs resolved in water and PVA) in the reservoir to get sucked in the air stream. Due to the air's high velocity the colloid is atomized in very tiny droplets.

The mixture of air and colloid droplets exits the airbrush pistol through a small nozzle and flies to the substrate. The small droplets dry usually immediately on impact preventing the substrate from getting wet and accumulating NDs in larger puddles.

Figure 20 (a) shows confocal scan of a conventional HDD head with clearly visible features of the writer. The actual write pole is located in the notch between two shield brackets (return front).

In Figure 20 (b) confocal scans are shown, after the ABS is air-brushed with NDs. The resulting distribution of NVs is much more homogeneous compared to the spin coating method (see Figure 19 d). For that reason, airbrush is used to apply NDs on the HAMR heads for temperature measurements.

In addition to the particle concentration the homogeneity of the resulting distribution of NDs is affected by the droplets size. In Germany airbrush pistols have to be designed in such a way, that the diameter of the droplets exceeds a few micrometers. Droplets of this size are too big to get into the pulmonary alveoli, if they are inhaled accidentally.

To improve the homogeneity further one could think about reducing the droplet size by using an atomizer designed for medical applications. Since for medical usage smaller droplets sizes are needed for moving active agents to the pulmonary alveoli. For this experiment the ND distribution of the airbrushed NDs seems to be sufficient.

### 9.5 CHARACTERIZATION OF NANODIAMONDS

Different kinds of NDs differ in PL and charge state stability as well as NV density and size. For all ND experiments stable NDs with a maximum diameter of about 50 nm diameter are used. To estimate the relation between dark and bright NDs a confocal scan (Figure 21 b) can be compared to an AFM (a) scan of the same area. Figure 21 (c) shows both scans on a spin coated glass substrate. By counting the number of bright spots corresponding to NVs in one or more NDs, it can be estimated that about 30 % of the NDs have bright NVs inside.

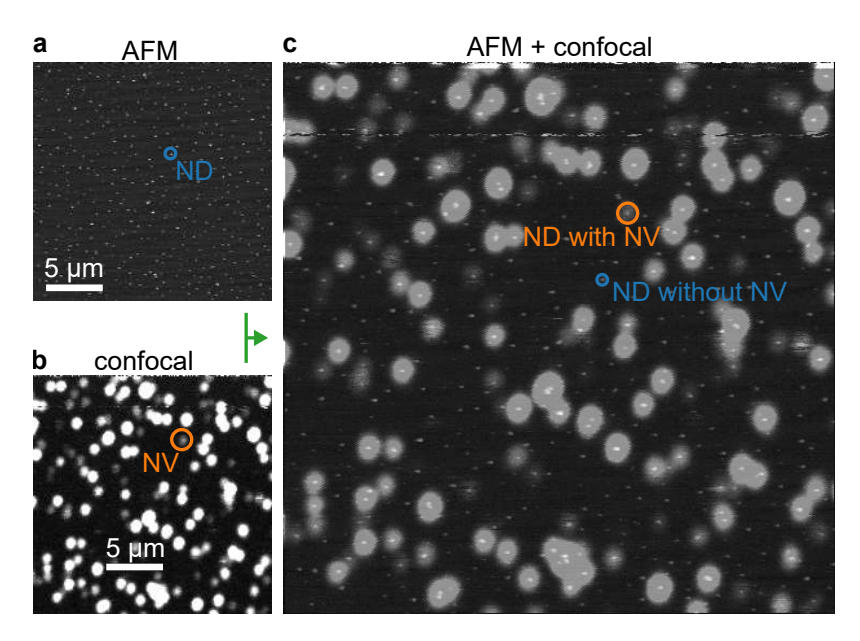


Figure 21: **a**, AFM scan of a glass substrate spin coated with NDs. Each dot represents a single ND. **b**, confocal scan of the same sector on the glass substrate. Each spot corresponds to a single or more NVs in an ND. **c**, Combination of AFM and confocal scan. By comparison it can be estimated that about 30 % of the NDs are bright.

#### NANOSCALE THERMOMETRY

For position dependent temperature measurements of the lollipop the NDs have to be in direct contact to the surface, homogeneously distributed in a region of about 1 µm² around the lollipop and individually addressable. The method of choice to achieve these requirements is the airbrush technique described in the last chapter with a colloid of water, PVA (ratio 1:1) and NDs with a maximum size of 50 nm.

#### 10.1 HAMR HEAD PREPARATION

The confocal scan in Figure 22 (a) shows the writer region of an untreated HAMR head. The bright spot at the top of the scan corresponds to the NFT. The PL counts of the NFT is greater by a factor of about 100 to 1000 compared to a single NV. The scan in (b) shows the same head after it is airbrushed with the colloid. The dots in the confocal scan corresponds to NVs. The density is large enough to cover the whole area, but simultaneously low enough to individually address single NDs.

Figure 22 (c) shows a photo of an airbrushed prototype HAMR head. The colorful reflections are interference effects by layers of PVA. The actual write head is located at the top of the picture.

The NDs lie directly on the ABS. This is why for all HAMR experiments a non-contact air microscopy objective is used instead of an oil objective. This comes with the disadvantage of collecting less photons due to the lower numerical aperture (NA).

### 10.2 PHOTO LUMINESCENCE OF THE NEAR FIELD TRANSDUCER

Like the structures on conventional HDD writers the writer of a HAMR device also shows PL when illuminated with a laser. Especially at the position of the NFT is a distinct bright spot in confocal scans.

Detail confocal scans (see Figure 23 a) around the NFT reveal two diffraction limited PL emitters spatially separated by about 500 nm. The emission depends heavily on the linear polarization of the excitation laser. For downtrack (corresponding to the tangent of a hard disk in an assembled drive) polarization (topmost scan) the left spot is brighter compared to the right one, whereby it is vice versa for the crosstrack (corresponding to the radial direction on a disk) polarization (bottommost scan). As expected both spots are excited when

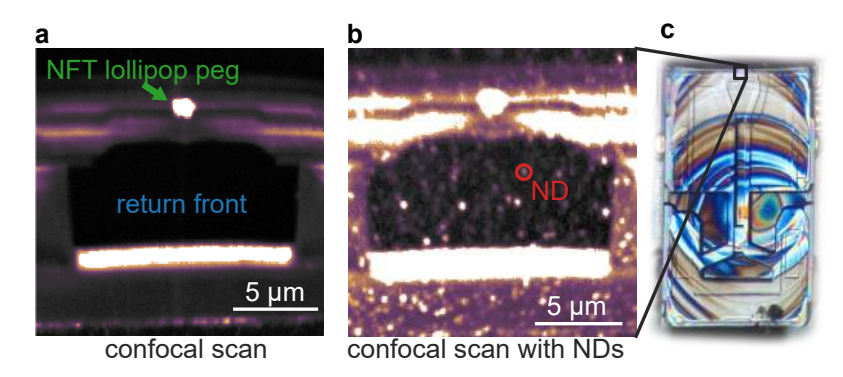


Figure 22: Airbrushed HAMR head. **a**, confocal scan of a HAMR head. The bright spot at the top of the scan corresponds to the NFT. **b**, same as (a), but after airbrushing with a water-PVA-ND-colloid. **c**, colorful reflections due to interference effects on an airbrushed HAMR head.

using a circular polarized excitation laser beam. The PL could either correspond to the NFT itself or to structures surrounding it.

In order to see the overlap of the NFT emission with the NV fluorescence spectra of a single NV and the NFT are recorded. In Figure 23 (b) it is clearly visible that both spectra overlap between about 700 nm and 770 nm. Due to the much higher brightness of the NFT a 700 nm low-pass filter is used to cut out most of the NFT's counts and keeping an acceptable number of NV counts at the detector. The drawback of this filter is that the signal strength at the APD is further reduced in addition to the air objective.

#### 10.3 RESULTS

A HAMR head prepared in the way described in the previous chapter can be used to measure the temperature of the NFT by using randomly distributed NDs. If the distance between ND and NFT is to large, the temperature of the ND is likely to be much lower than the NFT's tem-

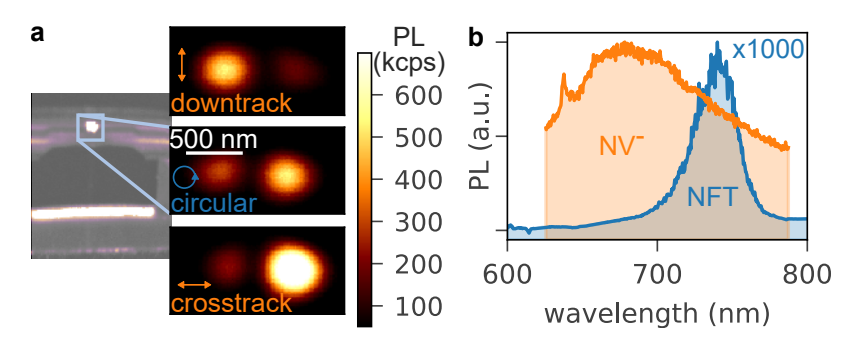


Figure 23: Investigation of the NFT's PL response. **a**, polarization dependence of the excitation laser. **b**, comparison of the emission spectra of an NV<sup>-</sup> and the NFT. The NFT is without a filter actually by a factor of 100 to 1000 brighter than a single NV.

perature. On the other hand, the NFT's fluorescence prevents measuring the NV's that are too close to the NFT. Ideally the distance between NV and NFT is in the same order of the resolution limit of the confocal microscope.

Figure 24 (a) shows a confocal scan of the region around the NFT. The bright spot in the center of the scan corresponds to the fluorescence of the NFT itself. Despite the low-pass filter the number of PL counts is still at least ten greater than the signal of a single NV.

The green marks in the scan correspond to one or more NVs in NDs. For the actual temperature measurements the two labeled NVs are used. The first NV (NV1) has a distance of about half a micrometer to the NFT. The distance to the write pole is with about 1  $\mu$ m even larger. For this NV a pure temperature shift is expected with almost no magnetic field effects.

The distance of the second NV (NV2) to the NFT is about a full micrometer and thus twice as large as for NV1. On the other hand the distance to the write pole is only half a micron. This NV should show a smaller or similar temperature shift but a much higher shift due to changes in the magnetic field.

In Figure 24 (b) the measurement sequence used to measure the shift is shown. As discussed in Section 9.1 the ND's ZFS cannot be determined by a single ODMR due to the remanence field and unknown strain in measurement. To separate the shifts induced by temperature variation from magnetic field effects and strain, the temperature is varied in a series of measurements by changing the duty cycle of the HAMR diode.

For longer duty cycles the temperature of the NFT and therefore also the temperature of the ND should increase and lead to parallel shift of both resonance lines to lower frequencies (see Figure 24 c). If not only the temperature changes but also the magnetic field, this can lead to additional splitting effects. Especially radial fields can induce parallel shifts of both lines, which can be mistaken for a temperature shift. NV1 should be dominated by temperature effects only, while for NV2 it is expected to show both temperature and magnetic field effects.

Figure 24 (d) finally shows the described measurement for NV1. Here, the duty cycle is increased from 0% to over 50% at a diode current of 27 mA. For the measurement a low voltage is applied at the writer to stabilize the magnetic field. The blue curve corresponds to the shift of the lower resonance line at 2.74 GHz while the orange curve corresponds to the resonance at 2.92 GHz. The grey curve describes the trend of the mean value of both lines. In a rough approximation the mean value indicates the pure temperature shift, if it is assumed that the magnetic field direction does not change.

Both lines show the expected shift to lower frequencies. At a duty cycle of 50% the ZFS decreased by about 3 MHz corresponding to a

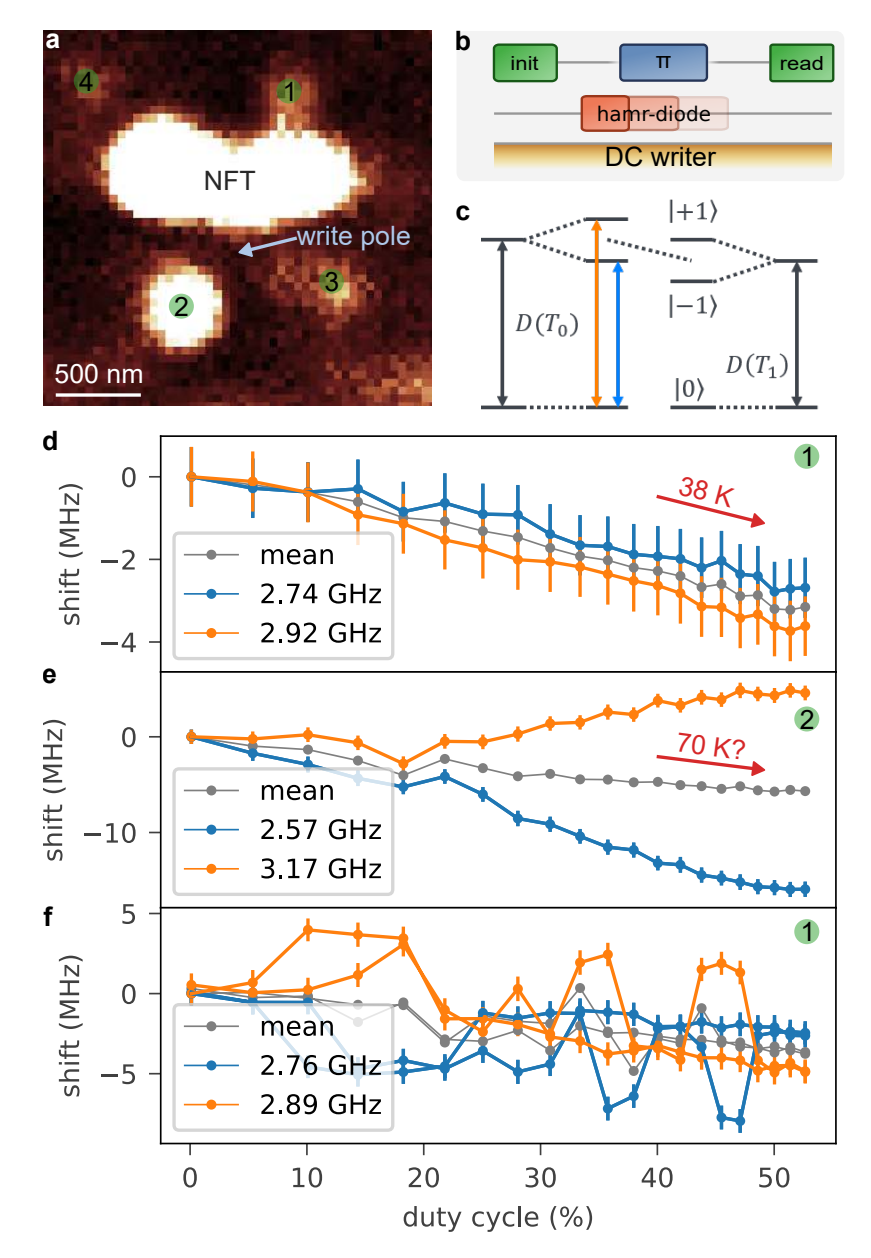


Figure 24: Results for ND based temperature measurements of the NFT. **a**, confocal scan of the region around the NFT. The two labeled NVs are used for the temperature measurements. **b**, pulse sequence for the measurement. The duty cycle of the HAMR diode is varied to expose the temperature effect. **c**, expected shift of the resonance lines induced by heating. **d**, measurement for NV1. **e**, measurement for NV2. **f**, measurement for NV1 with lower magnetic field.

temperature increase by about 38 K. The measured temperature shift is much lower compared to the theoretically predicted increase of several hundred degrees. Most likely this is due to the distance between NFT and ND or an insufficient heat transfer.

Part (e) of Figure 24 shows the results of the same measurement performed on NV2. The mean values show a similar shift to lower frequencies that indicates a decrease of the ZFS and therefore a higher temperature. Due to the shorter distance to the write pole the effect of the magnetic field leading to an additional splitting of the resonance lines, is greater compared to NV1. As we see a significant change in the axial field it cannot be simply assumed that the radial field did not change as well. Hence, an additional parallel shift of the resonances may add to the thermal effect, leading to an uncertain temperature measurement.

In Figure 24 (f) the importance of the static magnetic field during the measurement is demonstrated. The measurement is the same as shown in part (d) with a smaller voltage at the writer. This leads to a much more unstable magnetic field that reduces the accuracy of potential temperature measurements.

#### 10.4 OUTLOOK

A challenge for temperature sensors with nanoscale resolution is to confine the thermal contact to a nanoscale region and to restrict the heat dissipation through the sensor. Isolated NDs fulfill both requirements naturally. The presented measurements demonstrate in a proof of principle the thermal contact and reveal a temperature shift in dependence of the laser diode's duty cycle.

The coupling of the magnetic field is much stronger compared to the temperature induced shifts of the eigenenergies. Therefore the effect of magnetic field changes has to be eliminated to improve the precision of temperature measurements obtained by ODMR. The presence of eventually unaligned and drifting magnetic fields in combination with short coherence times close to the pole prevents also applying more complex measurement schemes based on interferometry [48, 49].

The coincidence of overlapping NV and NFT spectra affects every NV based sensor. For an accurate optical read-out of the electron spin the PL response can be separated spectrally, by lifetime and by optimizing the polarization of the excitation and detection. However, this is accompanied by smaller count rates leading to longer measurements times.

To achieve temperature mapping on the nanoscale one can consider of either moving the ND by pushing it with an AFM tip [50] or by attaching it directly to the tip [4]. This could lead to an NV based SThM

able to cover a wide broadband of temperatures with a nanoscale spatial resolution.

This thesis demonstrates, that the unique combination of properties of an HDD's writer is valuable for spin manipulation of the electron spin state in the NV center in diamond.

The high GHz bandwidth allows to switch and modulate the field created by the writer on a much faster timescale than a typical pulsed measurement schemes. This allows to create different pseudo static magnetic fields at distinct times during the measurement. This is helpful for the optical initialization and read-out when working with strong non-axial magnetic fields as demonstrated in this thesis.

External magnetic fields including microwave control fields are passively amplified close to the writer's position leading to a locally enhancement of the Rabi frequencies of almost three orders of magnitude. Thus Rabi oscillations can be driven with low signal powers preventing unwanted heating of the sample.

The large write field's amplitude combined with the high band-width allow to drive nonadiabatic fast passages. Whereas this thesis demonstrates the proof of principle further optimization could lead to extremely fast coherent gates on the order of 1 ns.

Radio or microwave radiation can be directly emitted by the writer, as well. The amplitudes generated in that way are orders of magnitude higher compared to conventional wire antennas. This can be used both to drive extraordinarily fast Rabi oscillations as well as to investigate non-linear effects of microwave-NV/HDD interaction. Especially nuclear spins typically require large amplitudes to be driven within relevant timescales. Here HDDs could enable double resonance experiments that would otherwise not be technically feasible.

Additionally the writer's field gradient can be used to selectively address NVs spectrally within a single diffraction limited spot independent of the NV orientation. In the future the same technique could be used to individually address the spins in a potential quantum register based on parallel dipolar coupled NVs. Also nanoscale MRI applications could profit from the large switchable magnetic field gradient of HDD writers. In this thesis the spectral addressing is used to optically determine the relative position of two parallel NVs with superresolution. The underlying DESM technique would not be applicable for parallel NVs with only macroscopic magnetic fields.

However, the usage of HDD writers for spin experiments does not come without drawbacks. The amplification of magnetic fields also applies to other fields present in the noise spectrum. This leads to drastic reductions of the transverse and longitudinal spin coherence times. As most of the advanced sensing sequences are based on the

observation of coherent phase evolution especially long transverse coherence times are essential. However, for certain constellations between NV and HDD transverse coherence can reach a few µs. This can already be sufficient for a large number of sensing protocols, but is a strong limitation on the sensitivity.

Further optimization is also needed for the positioning process. Due to the strong gradients even nanometer drifts of the writer can have immense effects on the system. Additionally the strong and often erratic behavior of the remanence magnetization has to be taken into account, as the spin dynamics cannot easily be controlled in an unknown and randomly changing environment. Essentially the writer should only be turned off for the initialization and read-out of the spin population in order to avoid the remanence magnetization. Even then, in close proximity to the pole the remanence fields can quench the NV fluorescence and contrast. In this case ODMR and hence the basis for NV measurements is not possible.

Finally it is investigated, whether the NV can be a valuable tool for the development of future HDD write heads using the HAMR technology. The NV embedded in NDs is hereby used as a nanoscale high-temperature sensor with the goal to examine the temperature of the heating elements of a prototype HAMR head. Bulk diamond and nanopillars do not present a suitable alternative to NDs due to the extraordinarily high heat dissipation. The relatively low total heating power of the HAMR head would quickly be distributed over a large bath and result in negligible equilibrium temperature.

NDs on the other hand are difficult to accurately position or evenly disperse on the nanoscale. Especially the profiled surface of the head prevents the use of standard methods for NDs distribution like spin coating. Instead a new method is tried by spraying the NDs with nanoscale homogeneity using an airbrush pistol.

Thermal shifts on the HAMR surface of tens of K are observed. They are, however, far below the expected several hundred Kelvins. The most likely explanation is, that the distance between NV and NFT is too large. Measurements close to the NFT are aggravated by its bright PL that spectrally overlaps with the NV's emission spectrum. Also temperature dependent magnetic field effects induced by the near write pole affect the temperature measurement.

Nevertheless, this thesis presents proofs of concept for the development of NV magnetometers and thermometers for the characterization of nanoscale devices. NV sensors now have the potential to fill a void in the miniaturization of hard disk drives and consequently contribute to satisfy the exponentially growing demand for data storage in the digital age.

# Part IV APPENDIX



### MAGNETIC FIELD RECONSTRUCTION

The magnetic field reconstruction for small magnetic fields is analytically solved in [12]. If the field amplitude is small the electron spin can be reliably initialized, since the  $|m_s=0\rangle$  state is only slightly disturbed for non-aligned and an eigenstate for aligned magnetic fields. In this case the resonances in the ODMR spectrum can easily be assigned to the spin state transitions.

Below the main results of [12] are cited, whereby the strain is neglected in this chapter. The notation is adjusted to the spin Hamiltonian given by Equation 1. For convenience the abbreviations  $\beta=\frac{\gamma_e}{2\pi}|B|$  and  $\Delta=\frac{\hbar}{2\pi}D\cos(2\theta)$  are used. Here  $|B|=\sqrt{B_x^2+B_y^2+B_z^2}$  is the absolute value of the magnetic field,  $\gamma_e=2\pi\cdot 28.02\,\text{GHz}\,\text{T}^{-1}$  the gyromagnetic ratio,  $\hbar=1.055\cdot 10^{-34}\,\text{J}$  s the reduced Planck constant,  $D=2.87\,\text{GHz}\cdot 2\pi\hbar^{-1}$  the ZFS and  $\theta=\arctan(B_\perp/B_z)$  the polar angle.

By solving the characteristic polynomial and matching the measured resonance frequencies  $\nu_1$  and  $\nu_2$  to the correct transitions  $\beta$  and  $\Delta$  can be expressed as functions of  $nu_1$  and  $nu_2$ 

$$\beta^2 = \frac{1}{3} \left( \nu_1^2 + \nu_2^2 - \nu_1 \nu_2 - D^2 \left( \frac{\hbar}{2\pi} \right)^2 \right)$$
 (12a)

$$\begin{split} \Delta = & \frac{7D^{3}\hbar^{3}(2\pi)^{-3} + 2(\nu_{1} + \nu_{2})(2(\nu_{1}^{2} + \nu_{2}^{2}) - 5\nu_{1}\nu_{2})}{9(\nu_{1}^{2} + \nu_{2}^{2} - \nu_{1}\nu_{2} - D^{2}\hbar^{2}(2\pi)^{-2})} \\ & - \frac{3D\hbar^{3}(2\pi)^{-3}(\nu_{1}^{2} + \nu_{2}^{2} - \nu_{1}\nu_{2})}{9(\nu_{1}^{2} + \nu_{2}^{2} - \nu_{1}\nu_{2} - D^{2}\hbar^{2}(2\pi)^{-2})} \end{split} \tag{12b}$$

By using the definitions for  $\beta$  and  $\Delta$  the absolute value of the magnetic field |B| and the polar angle  $\theta$  can be reconstructed.

For strong magnetic fields the reconstruction in this thesis is performed numerically by fitting the Hamiltonian to the observed resonances. Hereby it is assumed, that the spin state is initialized to  $m_{\rm s}=0$  at zero field. If the field is ramped up slowly, such that an adiabatic behavior can be assumed, the spin ends up in the lowest eigenstate.

The observed resonances then correspond to transitions between the lowest to the middle or topmost level. The free parameters of the Hamiltonian (i. e. the three magnetic field components) are now varied to minimize the difference between the observed resonances to the calculated transition frequencies. In principle this process can also be solved analytically. However, the numerical solution is entirely sufficient for the field reconstruction in this thesis.

### HARMONIC GENERATION

The non-linear relation between the magnetization M and magnetic field H can be described by

$$\mathbf{M} = \sum_{n} \chi^{(n)} \mathbf{H}^{n} = \chi^{(1)} \mathbf{H} + \chi^{(2)} \mathbf{H}^{2} + \chi^{(3)} \mathbf{H}^{3} + \dots , \qquad (13)$$

where  $\chi^n$  are the  $n^{th}$  order magnetic susceptibilities of the material, if the ferromagnetic hysteresis is not taken into account. The magnetic susceptibilities  $\chi^{(n)}$  are here tensors of the order n+1. This description is analogous to the nonlinear description of the electric field in non-linear optics.

#### B.1 SECOND AND THIRD HARMONIC GENERATION

If an external, sinusoidal and linear polarized (e.g. along the x direction) magnetic H-field  $\mathbf{H}(t) = H_0 \sin(\omega t) \mathbf{e}_x$  of the frequency  $\omega$  is applied the magnetization is given by

$$\label{eq:mass} \begin{split} \boldsymbol{M}(t) = \chi_x^{(1)} H_0 \sin(\omega t) + \chi_{xx}^{(2)} H_0^2 \sin^2(\omega t) + \chi_{xxx}^{(3)} H_0^3 \sin^3(\omega t) + \dots \ . \end{split}$$

Using the two trigonometric identities

$$\sin^2(x) = \frac{1}{2} - \frac{1}{2}\sin(2x) \tag{15a}$$

$$\sin^3(x) = \frac{3}{4}\sin(x) - \frac{1}{4}\sin(3x) \tag{15b}$$

leads to the magnetization

$$\begin{split} \mathbf{M}(t) = & \frac{\chi_{xx}^{(2)} H_0}{2} + \left(\chi_x^{(1)} H_0 + \frac{3\chi_{xxx}^{(3)} H_0^3}{4}\right) \sin(\omega t) \\ & - \frac{\chi_{xx}^{(2)} H_0^2}{2} \sin(2\omega t) - \frac{\chi_{xxx}^{(3)} H_0^3}{4} \sin(3\omega t) + \dots \; . \end{split} \tag{16}$$

Due to the non-linearity of the magnetic susceptibility terms oscillating with  $2\omega$  and  $3\omega$  appear. This is called second and third harmonic generation. If terms of a higher order are taken into account too, even higher harmonics appear. The amplitude of the terms scale with the second respectively third power of the magnetic field amplitude  $H_0$ .

#### B.2 DIFFERENCE AND SUM FREQUENCY GENERATION

For the difference and sum frequency generation the second order susceptibility is sufficient. Therefore the third order term is omitted for simplicity in this section.

If a magnetic field

$$\mathbf{H}(t) = \mathbf{H}_0 \left( \sin(\omega_1 t) + \sin(\omega_2 t) \right) \mathbf{e}_{\mathbf{x}} \tag{17}$$

with two sinusoidal components of different frequencies  $\omega_1$  and  $\omega_2$  is applied (same amplitude  $H_0$  for simplicity), the magnetization is given by

$$\begin{split} \mathbf{M}(t) = & \chi_{x}^{(1)} H_{0} \left( \sin(\omega_{1}t) + \sin(\omega_{2}t) \right) \\ & + \chi_{xx}^{(2)} H_{0}^{2} \left( \sin(\omega_{1}t) + \sin(\omega_{2}t) \right)^{2} \\ = & \chi_{x}^{(1)} H_{0} \left( \sin(\omega_{1}t) + \sin(\omega_{2}t) \right) \\ & + \chi_{xx}^{(2)} H_{0}^{2} \left( \sin^{2}(\omega_{1}t) + \sin^{2}(\omega_{2}t) \right) \\ & + \chi_{xx}^{(2)} H_{0}^{2} \left( 2\sin(\omega_{1}t) \sin(\omega_{2}t) \right) \end{split} \tag{18}$$

By using the trigonometric identity

$$\sin(x)\sin(y) = \frac{\cos(x-y)}{2} - \frac{\cos(x+y)}{2} \tag{19}$$

and again Equation 15b this leads to the magnetization

$$\begin{split} \mathbf{M}(t) = & \chi_{xx}^{(2)} H_0 \\ & + \chi_x^{(1)} H_0 \sin(\omega_1 t) + \chi_x^{(1)} H_0 \sin(\omega_2 t) \\ & - \frac{\chi_{xx}^{(2)} H_0^2}{2} \sin(2\omega_1 t) - \frac{\chi_{xx}^{(2)} H_0^2}{2} \sin(2\omega_2 t) \\ & + \chi_{xx}^{(2)} H_0^2 \cos\left((\omega_1 - \omega_2)t\right) - \chi_{xx}^{(2)} H_0^2 \cos\left((\omega_1 + \omega_2)t\right) \end{split} \tag{20}$$

with terms oscillating with the difference  $\omega_1 - \omega_2$  and the sum  $\omega_1 + \omega_2$  of the initial frequencies. These effects are called difference and sum frequency generation.

- [1] W. Pfaff, B. J. Hensen, H. Bernien, S. B. van Dam, M. S. Blok, T. H. Taminiau, M. J. Tiggelman, R. N. Schouten, M. Markham, D. J. Twitchen, and R. Hanson, "Unconditional quantum teleportation between distant solid-state quantum bits," Science (New York, N.Y.) 345, 532–535 (2014).
- [2] G. Waldherr, P. Neumann, S. F. Huelga, F. Jelezko, and J. Wrachtrup, "Violation of a temporal bell inequality for single spins in a diamond defect center," Physical review letters 107, 090401 (2011).
- [3] G. Waldherr, Y. Wang, S. Zaiser, M. Jamali, T. Schulte-Herbrüggen, H. Abe, T. Ohshima, J. Isoya, J. F. Du, P. Neumann, and J. Wrachtrup, "Quantum error correction in a solid-state hybrid spin register," Nature **506**, 204–207 (2014).
- [4] A. Laraoui, H. Aycock-Rizzo, Y. Gao, X. Lu, E. Riedo, and C. A. Meriles, "Imaging thermal conductivity with nanoscale resolution using a scanning spin probe," Nature communications 6, 8954 (2015).
- [5] J. Michl, T. Teraji, S. Zaiser, I. Jakobi, G. Waldherr, F. Dolde, P. Neumann, M. W. Doherty, N. B. Manson, J. Isoya, and J. Wrachtrup, "Perfect alignment and preferential orientation of nitrogen-vacancy centers during chemical vapor deposition diamond growth on (111) surfaces," Applied Physics Letters 104, 102407 (2014).
- [6] J. P. Tetienne, T. Hingant, J.-V. Kim, L. H. Diez, J.-P. Adam, K. Garcia, J.-F. Roch, S. Rohart, A. Thiaville, D. Ravelosona, and V. Jacques, "Nanoscale imaging and control of domain-wall hopping with a nitrogen-vacancy center microscope," Science (New York, N.Y.) 344, 1366–1369 (2014).
- [7] J. F. Barry, M. J. Turner, J. M. Schloss, D. R. Glenn, Y. Song, M. D. Lukin, H. Park, and R. L. Walsworth, "Optical magnetic detection of single-neuron action potentials using quantum defects in diamond," Proceedings of the National Academy of Sciences of the United States of America 113, 14133–14138 (2016).
- [8] G. Kucsko, P. C. Maurer, N. Y. Yao, M. Kubo, H. J. Noh, P. K. Lo, H. Park, and M. D. Lukin, "Nanometre-scale thermometry in a living cell," Nature **500**, 54–58 (2013).

- [9] S. Steinert, F. Ziem, L. T. Hall, A. Zappe, M. Schweikert, N. Götz, A. Aird, G. Balasubramanian, L. Hollenberg, and J. Wrachtrup, "Magnetic spin imaging under ambient conditions with subcellular resolution," Nature communications 4, 1607 (2013).
- [10] M. W. Doherty, N. B. Manson, P. Delaney, F. Jelezko, J. Wrachtrup, and L. C. L. Hollenberg, "The nitrogen-vacancy colour centre in diamond," Physics Reports **528**, 1–45 (2013).
- [11] T. Wolf, P. Neumann, K. Nakamura, H. Sumiya, T. Ohshima, J. Isoya, and J. Wrachtrup, "Subpicotesla diamond magnetometry," Physical Review X 5 (2015).
- [12] G. Balasubramanian, I. Y. Chan, R. Kolesov, M. Al-Hmoud, J. Tisler, C. Shin, C. Kim, A. Wojcik, P. R. Hemmer, A. Krueger, T. Hanke, A. Leitenstorfer, R. Bratschitsch, F. Jelezko, and J. Wrachtrup, "Nanoscale imaging magnetometry with diamond spins under ambient conditions," Nature 455, 648–651 (2008).
- [13] F. Dolde, H. Fedder, M. W. Doherty, T. Nöbauer, F. Rempp,
  G. Balasubramanian, T. Wolf, F. Reinhard, L. C. L. Hollenberg,
  F. Jelezko, and J. Wrachtrup, "Electric-field sensing using single diamond spins," Nature Physics 7, 459–463 (2011).
- [14] T. Rendler, J. Neburkova, O. Zemek, J. Kotek, A. Zappe, Z. Chu, P. Cigler, and J. Wrachtrup, "Optical imaging of localized chemical events using programmable diamond quantum nanosensors," Nature communications 8, 14701 (2017).
- [15] P. Neumann, I. Jakobi, F. Dolde, C. Burk, R. Reuter, G. Waldherr, J. Honert, T. Wolf, A. Brunner, and J. H. Shim, "High-precision nanoscale temperature sensing using single defects in diamond," Nano letters 13, 2738–2742 (2013).
- [16] T. Staudacher, F. Shi, S. Pezzagna, J. Meijer, J. Du, C. A. Meriles, F. Reinhard, and J. Wrachtrup, "Nuclear magnetic resonance spectroscopy on a (5-nanometer)3 sample volume," Science (New York, N.Y.) 339, 561–563 (2013).
- [17] N. Aslam, M. Pfender, P. Neumann, R. Reuter, A. Zappe, F. Fávaro de Oliveira, A. Denisenko, H. Sumiya, S. Onoda, J. Isoya, and J. Wrachtrup, "Nanoscale nuclear magnetic resonance with chemical resolution," Science (New York, N.Y.) 357, 67–71 (2017).
- [18] M. S. Grinolds, M. Warner, K. de Greve, Y. Dovzhenko, L. Thiel, R. L. Walsworth, S. Hong, P. Maletinsky, and A. Yacoby, "Subnanometre resolution in three-dimensional magnetic resonance imaging of individual dark spins," Nature nanotechnology 9, 279–284 (2014).

- [19] B. Grotz, M. V. Hauf, M. Dankerl, B. Naydenov, S. Pezzagna, J. Meijer, F. Jelezko, J. Wrachtrup, M. Stutzmann, F. Reinhard, and J. A. Garrido, "Charge state manipulation of qubits in diamond," Nature communications 3, 729 (2012).
- [20] M. Pfender, N. Aslam, P. Simon, D. Antonov, G. Thiering, S. Burk, F. Fávaro de Oliveira, A. Denisenko, H. Fedder, J. Meijer, J. A. Garrido, A. Gali, T. Teraji, J. Isoya, M. W. Doherty, A. Alkauskas, A. Gallo, A. Grüneis, P. Neumann, and J. Wrachtrup, "Protecting a diamond quantum memory by charge state control," Nano letters 17, 5931–5937 (2017).
- [21] A. Lenef and S. C. Rand, "Electronic structure of the n- v center in diamond: Theory," Physical Review B **53**, 13441–13455 (1996).
- [22] A. Gruber, A. Dräbenstedt, C. Tietz, L. Fleury, J. Wrachtrup, and C. von Borczyskowski, "Scanning confocal optical microscopy and magnetic resonance on single defect centers," Science (New York, N.Y.) 276, 2012–2014 (1997).
- [23] I. Jakobi, P. Neumann, Y. Wang, D. B. R. Dasari, F. El Hallak, M. A. Bashir, M. Markham, A. Edmonds, D. Twitchen, and J. Wrachtrup, "Measuring broadband magnetic fields on the nanoscale using a hybrid quantum register," Nature nanotechnology 12, 67–72 (2017).
- [24] X.-F. He, N. B. Manson, and P. T. H. Fisk, "Paramagnetic resonance of photoexcited n- v defects in diamond. ii. hyperfine interaction with the n14 nucleus," Physical Review B 47, 8816–8822 (1993).
- [25] M. Steiner, P. Neumann, J. Beck, F. Jelezko, and J. Wrachtrup, "Universal enhancement of the optical readout fidelity of single electron spins at nitrogen-vacancy centers in diamond," Physical Review B 81 (2010).
- [26] N. B. Manson, J. P. Harrison, and M. J. Sellars, "Nitrogen-vacancy center in diamond: Model of the electronic structure and associated dynamics," Physical Review B 74, 664 (2006).
- [27] J. P. Tetienne, L. Rondin, P. Spinicelli, M. Chipaux, T. Debuisschert, J.-F. Roch, and V. Jacques, "Magnetic-field-dependent photodynamics of single nv defects in diamond: An application to qualitative all-optical magnetic imaging," New Journal of Physics 14, 103033 (2012).
- [28] R. J. Epstein, F. M. Mendoza, Y. K. Kato, and D. D. Awschalom, "Anisotropic interactions of a single spin and dark-spin spectroscopy in diamond," Nature Physics 1, 94–98 (2005).

- [29] M. W. Doherty, J. Michl, F. Dolde, I. Jakobi, P. Neumann, N. B. Manson, and J. Wrachtrup, "Measuring the defect structure orientation of a single nv centre in diamond," New Journal of Physics 16, 063067 (2014).
- [30] D. M. Toyli, D. J. Christle, A. Alkauskas, B. B. Buckley, C. G. van de Walle, and D. D. Awschalom, "Measurement and control of single nitrogen-vacancy center spins above 600k," Physical Review X 2, 11 (2012).
- [31] S. K. Khizroev, M. H. Kryder, Y. Ikeda, K. Rubin, P. Arnett, M. Best, and D. A. Thompson, "Recording heads with track widths suitable for 100 gbit/in<sup>2</sup> density," IEEE Transactions on Magnetics 35, 2544–2546 (1999).
- [32] D. Reinsel, J. Gantz, and J. Rydning, "Data age 2025: The evolution of data to life-critical: Don't focus on big fata; focus on the data that's big: An idc white paper, sponsored by seagate," https://www.seagate.com/files/www-content/our-story/trends/files/Seagate-WP-DataAge2025-March-2017.pdf.
- [33] Association of Science Technology Centers, "ASTC technology roadmap," (2016). http://idema.org/?page\_id=5868.
- [34] A. Moser, K. Takano, D. T. Margulies, M. Albrecht, Y. Sonobe, Y. Ikeda, S. Sun, and E. E. Fullerton, "Magnetic recording advancing into the future," Journal of Physics D: Applied Physics 35, R157–R167 (2002).
- [35] J.-G. Zhu, X. Zhu, and Y. Tang, "Microwave assisted magnetic recording," IEEE Transactions on Magnetics 44, 125–131 (2008).
- [36] R. E. Rottmayer, S. Batra, D. Buechel, W. A. Challener, J. Hohlfeld, Y. Kubota, L. Li, B. Lu, C. Mihalcea, K. Mountfield, K. Pelhos, C. Peng, T. Rausch, M. A. Seigler, D. Weller, and X.-M. Yang, "Heat-assisted magnetic recording," IEEE Transactions on Magnetics 42, 2417–2421 (2006).
- [37] D. Jiles, *Introduction to magnetism and magnetic materials* (Chapman & Hall, London u.a, 1998), 2nd ed.
- [38] J.-P. Tetienne, T. Hingant, L. Rondin, A. Cavaillès, L. Mayer, G. Dantelle, T. Gacoin, J. Wrachtrup, J.-F. Roch, and V. Jacques, "Spin relaxometry of single nitrogen-vacancy defects in diamond nanocrystals for magnetic noise sensing," Physical Review B 87 (2013).
- [39] H. Zhang, K. Arai, C. Belthangady, J.-C. Jaskula, and R. L. Walsworth, "Selective addressing of solid-state spins at the nanoscale via magnetic resonance frequency encoding," npj Quantum Information 3, 38 (2017).

- [40] E. H. Chen, O. Gaathon, M. E. Trusheim, and D. Englund, "Wide-field multispectral super-resolution imaging using spin-dependent fluorescence in nanodiamonds," Nano letters 13, 2073–2077 (2013).
- [41] I. Jakobi, S. A. Momenzadeh, F. F. de Oliveira, J. Michl, F. Ziem, M. Schreck, P. Neumann, A. Denisenko, and J. Wrachtrup, "Efficient creation of dipolar coupled nitrogen-vacancy spin qubits in diamond," Journal of Physics: Conference Series 752, 012001 (2016).
- [42] R. W. Boyd, *Nonlinear optics* (Elsevier/Academic Press, Amsterdam, 2008), 3rd ed.
- [43] L. D. Landau and E. M. Lifšic, *Quantum mechanics: Non-relativistic theory*, vol. / by L. D. Landau and E. M. Lifshitz; Vol. 3 of *Course of theoretical physics* (Elsevier, Singapore, 2007), 3rd ed.
- [44] P. Maletinsky, S. Hong, M. S. Grinolds, B. Hausmann, M. D. Lukin, R. L. Walsworth, M. Loncar, and A. Yacoby, "A robust scanning diamond sensor for nanoscale imaging with single nitrogen-vacancy centres," Nature nanotechnology 7, 320–324 (2012).
- [45] W. A. Challener, C. Peng, A. V. Itagi, D. Karns, W. Peng, Y. Peng, X. Yang, X. Zhu, N. J. Gokemeijer, Y.-T. Hsia, G. Ju, R. E. Rottmayer, M. A. Seigler, and E. C. Gage, "Heat-assisted magnetic recording by a near-field transducer with efficient optical energy transfer," Nature Photonics 3, 220–224 (2009).
- [46] S. A. Momenzadeh, R. J. Stohr, F. F. de Oliveira, A. Brunner, A. Denisenko, S. Yang, F. Reinhard, and J. Wrachtrup, "Nanoengineered diamond waveguide as a robust bright platform for nanomagnetometry using shallow nitrogen vacancy centers," Nano letters 15, 165–169 (2015).
- [47] C. E. Walker, Z. Xia, Z. S. Foster, B. J. Lutz, and Z. H. Fan, "Investigation of airbrushing for fabricating microelectrodes in microfluidic devices," Electroanalysis 20, 663–670 (2008).
- [48] J. Wang, F. Feng, J. Zhang, J. Chen, Z. Zheng, L. Guo, W. Zhang, X. Song, G. Guo, L. Fan, C. Zou, L. Lou, W. Zhu, and G. Wang, "High-sensitivity temperature sensing using an implanted single nitrogen-vacancy center array in diamond," Physical Review B 91 (2015).
- [49] D. M. Toyli, C. F. de las Casas, D. J. Christle, V. V. Dobrovitski, and D. D. Awschalom, "Fluorescence thermometry enhanced by the quantum coherence of single spins in diamond," Proceedings of the National Academy of Sciences of the United States of America 110, 8417–8421 (2013).

[50] A. W. Schell, G. Kewes, T. Schröder, J. Wolters, T. Aichele, and O. Benson, "A scanning probe-based pick-and-place procedure for assembly of integrated quantum optical hybrid devices," The Review of scientific instruments 82, 073709 (2011).

## **DECLARATION**

Ich versichere,

- dass ich diese Masterarbeit selbstständig verfasst habe,
- dass ich keine anderen als die angegebenen Quellen benutzt und alle wörtlich oder sinngemäß aus anderen Werken übernommenen Aussagen als solche gekennzeichnet habe,
- dass die eingereichte Arbeit weder vollständig noch in wesentlichen Teilen Gegenstand eines anderen Prüfungsverfahren gewesen ist,
- und dass das elektronische Exemplar mit den gedruckten Exemplaren übereinstimmt.

Sven Bodenstedt